Journal of Nuclear Materials 405 (2010) 216–234

Contents lists available at ScienceDirect

Journal of Nuclear Materials

journal homepage: www.elsevier.com/locate/jnucmat

Ab initio-based diffusion theory and tracer diffusion in Ni–Cr and Ni–Fe alloys

J.D. Tucker [a,b], R. Najafabadi [b], T.R. Allen [c], D. Morgan [d,*]

[a] University of Wisconsin–Madison, 1500 Engineering Drive, Madison, WI 53706, USA
[b] Knolls Atomic Power Laboratory, P.O. Box 1072, Schenectady, NY 12301, USA
[c] University of Wisconsin–Madison, Department of Nuclear Engineering and Engineering Physics, 1500 Engineering Drive, Madison, WI 53706, USA
[d] University of Wisconsin–Madison, 1509 University Ave., Madison, WI 53706, USA

ARTICLE INFO

Article history:
Received 5 August 2009
Accepted 5 August 2010

ABSTRACT

In this paper, *ab initio* modeling is used to predict diffusion relevant thermodynamic and kinetic information for dilute Ni–Cr and Ni–Fe alloys. The modeling results are then used to determine the phenomenological coefficient matrices and the tracer diffusion coefficients for both vacancy and interstitial mediated diffusion. In addition to predicting diffusion coefficients, this *ab initio*-based approach provides information typically inaccessible to experiments, including the different contributions to diffusion (e.g., electronic excitation effects), the species dependence of interstitial diffusion, and the deviations from Arrhenius-type relations, which are often used to describe and extrapolate experimental diffusion data. It is found that: (1) Cr is the fastest diffusing species in Ni by both vacancy and interstitial diffusion, followed by Fe and then Ni. The enhanced diffusivity of Cr is primarily due to differences in migration barriers and binding energies, not pre-exponential factors. (2) Fe and Cr solutes in Ni have weak interactions with vacancies but Cr solutes bind strongly to interstitial defects. (3) Cr exhibits non-Arrhenius behavior in both vacancy and interstitial mediated diffusion. (4) Temperature dependent electronic contributions have a significant impact on the diffusion in some cases. (5) The vacancy diffusion mechanism in Ni–Cr changes as a function of temperature resulting in vacancy–solute drag below 460 K.

1. Introduction

Ab initio techniques provide a powerful method for obtaining detailed point defect energetics and are increasingly used to study the diffusion of elements in pure metals and multi-component alloys [1,2]. In this paper *ab initio* techniques are used to calculate tracer diffusion coefficients, for both vacancy and interstitial mediated diffusion, in the dilute Ni–Cr and Ni–Fe alloys. The Ni–Cr–Fe system is an important model alloy for Ni-based alloys and austenitic steels and, despite many years of study, there is still significant uncertainly about the diffusion coefficients in these systems. Point defect diffusion is particularly important in Ni–Cr–Fe steels as these materials are commonly used in the nuclear industry, where irradiation creates both vacancy and interstitial defects in the matrix. The diffusion of these defects then leads to many microstructural and microchemical changes [3,4], from void growth [5] to radiation-induced segregation [6], the effects of which must be understood for reliable application of these materials in next generation reactors.

The purpose of this paper is twofold. The first purpose is to provide tracer diffusion coefficients and point defect thermokinetic data in the technologically important Ni–Cr–Fe system. *Ab initio*-based modeling allows for the determination of diffusion properties that are challenging to investigate experimentally. For vacancy diffusion there is extensive experimental data, but generally only at high temperatures. Extrapolation to lower temperature is typically done by fitting to an Arrhenius expression of the form $D = D_0 e^{-Q/kT}$, where the pre-exponential factor, D_0, and activation energy, Q, are assumed to be constants. *Ab initio* modeling can be used to determine accurate temperature dependent values of D_0 and Q, reducing uncertainty in the experimental determination and allowing much more reliable extrapolation to lower temperatures. *Ab initio* modeling can predict coupling between the transport of solute and defect species (e.g., vacancy–solute drag) that is difficult to assess experimentally. Finally, experimental self-interstitial diffusion properties in Ni–Cr–Fe alloys are rare and *ab initio* techniques are increasingly being utilized to provide these data [7,8].

The second purpose of this paper is to provide a framework for propagating point defect energetics through a rate expression and into statistical mechanics models to determine the kinetic phenomenological coefficient matrix (e.g., propagating vibrational excitations through Lidiard and LeClaire's five-frequency model [9,10]). The phenomenological coefficient matrix can be used to

* Corresponding author. Tel.: +1 608 265 5879; fax: +1 608 262 8353.
E-mail addresses: jdtucker@wisc.edu, julie.tucker@unnpp.gov (J.D. Tucker), najafab@kapl.gov (R. Najafabadi), allen@engr.wisc.edu (T.R. Allen), ddmorgan@wisc.edu (D. Morgan).

0022-3115/$ - see front matter © 2010 Elsevier B.V. All rights reserved.
doi:10.1016/j.jnucmat.2010.08.003

calculate diffusion coefficients and fluxes, which are needed to study various transport related phenomena. The methods used in this framework have all been derived separately in different contexts, and are integrated here for clarity and application to irradiated materials. The individual steps in this framework are often approximated in order to compensate for insufficient experimental data. *Ab initio* techniques provide detailed information that was unavailable experimentally, and statistical mechanics based models can now be parameterized with complete sets of energetic data, removing the approximations needed in the past.

Section 2 of this paper discusses the overall methodology in which the tracer diffusion coefficients were obtained, with the details provided in Appendices A–D. The *ab initio* techniques used in this work and the settings associated with them are also discussed in Section 2. Section 3.1 presents the results for vacancy mediated diffusion. The diffusion coefficients are compared to experimental results and the differences are discussed. The temperature dependence of pre-exponential factor terms in the diffusion coefficients are illustrated and explained. This section also presents the results of the vacancy wind calculation, which describes the temperature dependence of the migration mechanism. Finally, an assessment of the error associated with the Arrhenius fit to diffusion data is presented. Section 3.2 presents the calculated interstitial mediated diffusion coefficients and provides comparison with the vacancy mediated results. This section also assesses the temperature dependence of pre-exponential factor terms and the error of the Arrhenius fit for interstitial diffusion data. Section 3.3 presents a brief discussion of implications of the *ab initio* predictions for radiation-induced segregation. Finally, Section 4 gives a summary of the key results. Numerous technical details have been excluded from the main text for clarity, but are provided in the appendices.

2. Methodology

2.1. Overview of approach

In this work, tracer diffusion coefficients for vacancy and interstitial mediated diffusion are calculated in the Ni–Cr and Ni–Fe binaries through a multi-step process. The process to obtain these diffusion coefficients uses *ab initio* methods to calculate migration rates and thermodynamic parameters. These rates are then used to calculate phenomenological coefficients, which are kinetic quantities that describe the mobility of the elemental species and point defects. The phenomenological coefficients are, in turn, used to calculate tracer diffusion coefficients and the vacancy wind, which identifies the coupling between vacancy and solute fluxes.

The coupling between migration rates, phenomenological coefficients and diffusion coefficients, the *ab initio* generated thermokinetic data, and the approximations used throughout the process of obtaining the diffusion coefficients, have been provided in the appendix for the interested reader. For derivations of the relationships used the reader is referred to the original references. Appendix A provides a rate expression, based on the Eyring–Polanyi equation [11,12] and transition state theory, that includes vibrational and electronic excitation contributions. Appendix B outlines the process of using the rates of various hopping events to obtain the phenomenological coefficients. The phenomenological coefficients describe the mobility of each species in a dilute binary alloy and are used to calculate intrinsic diffusion coefficients. The steps to obtain the tracer diffusion coefficients from the intrinsic diffusion coefficients and the method to incorporate the vibrational and electronic excitation contributions of defect–solute binding in the tracer diffusion coefficients are given in Appendix C. The thermokinetic data generated by *ab initio* calculations needed to calculate the phenomenological coefficient matrix and the tracer diffusion coefficients are given in Appendix D.

2.2. Ab initio methods

Ab initio calculations are used in this work to determine migration barriers, binding enthalpies, electronic density of states, lattice constants, vibrational frequencies and defect formation enthalpies for the Ni–Cr and Ni–Fe systems. While some *ab initio* defect properties in Ni systems have been calculated in the past [1,13,14], additional defect properties are needed for this work and the values available in the literature have been recalculated for consistency.

All *ab initio* calculations were performed with the Vienna *Ab initio* Simulation Package (VASP) [15,16], a quantum mechanical code based on density functional theory. All VASP calculations were performed with the generalized gradient approximation (GGA) for the exchange–correlation energy, the Perdew–Burke–Ernzerhof exchange–correlation functional [17] and the projector-augmented wave method [18,19] unless stated otherwise. The calculations were performed with a 96(±1) or 108(±1) atom periodic simulation cell. The volume and shape of each simulation cell was fixed but ionic relaxations were allowed within the cell. Migration barriers and vibrational frequencies were calculated with a 270 eV energy cutoff and a $3 \times 3 \times 3k$-point mesh. Binding energies and electronic density of states calculations were computed with a 479 eV cutoff and a $4 \times 4 \times 4k$-point mesh. The cumulative errors associated with k-point mesh, energy cutoff and cell size convergence are estimated to be less than 35 meV for migration barriers, defect formation energies and binding energies when added in quadrature [20]. All calculations were spin polarized and allowed for magnetic ordering. Interstitial migration barriers are determined by the nudged elastic band method [21]. Vacancy migration barriers are determined from constrained calculations with the hopping atom restricted to a plane perpendicular to the migration pathway but all other ionic relaxations are allowed. This method gives comparable results to the nudged elastic band method for all cases tested.

3. Results and discussion

The methods outlined in Section 2 and the data presented in Appendix D have been used to calculate both vacancy and interstitial mediated tracer diffusion coefficients for Ni self-diffusion and dilute Cr and Fe impurity diffusion in Ni.

3.1. Vacancy mediated diffusion

The parameters needed for vacancy mediated tracer diffusion are summarized in Table 1. All values are determined using *ab initio* methods, as discussed in more detail in the appendices. The Ni self-diffusion and Cr and Fe tracer diffusion coefficients in Ni have been calculated from Eqs. (C.12) and (C.16), using the parameters from Table 1. Each *ab initio*-based diffusion constant is compared to multiple sets of Arrhenius fits to experimental diffusion data in Figs. 1–3. The experimental data contains both single crystal and polycrystalline diffusion data and the reported purities of the Ni in Askill [22] and Smithells [23] are 99.9% and above for both self and impurity tracer diffusion.

Figs. 1–3 show that the *ab initio* diffusion data predict values lower than the main cluster of experimental diffusion coefficients by approximately an order of magnitude. However, the temperature dependence of the diffusion coefficients and the relative ordering between the different species is represented well. The differences between the *ab initio* calculated and experimental

Table 1
Parameters for vacancy mediated tracer diffusion.

Parameter	Value	Units
Ni parameters		
a	0.35239	nm
S_{vf}	1.82	k_B
H_{vf}	1.65	eV
ν_{mig} Ni	4.48×10^{12}	Hz
Ni DOS (TS–OL)	−0.66	states/eV/cell
ΔH_{mig} w_0	1.09	eV
Cr in Ni parameters		
ν_{mig} Cr	4.92×10^{12}	Hz
Cr DOS (TS–OL)	0.61	states/eV/cell
H_{bind} Cr_v	0.05	eV
ν_{bind} Cr_v	1.25	N/A
Cr DOS (OL–∞)	0.76	states/eV/cell
ΔH_{mig} w_1	0.98	eV
ΔH_{mig} w_2	0.83	eV
ΔH_{mig} w_3	1.04	eV
ΔH_{mig} w_4	1.06	eV
Fe in Ni parameters		
ν_{mig} Fe	4.14×10^{12}	Hz
Fe DOS (TS–OL)	−0.43	states/eV/cell
H_{bind} Fe_v	0.02	eV
ν_{bind} Fe_v	1.29	N/A
Fe DOS (OL–∞)	0.44	states/eV/cell
ΔH_{mig} w_1	1.13	eV
ΔH_{mig} w_2	0.97	eV
ΔH_{mig} w_3	1.07	eV
ΔH_{mig} w_4	1.07	eV

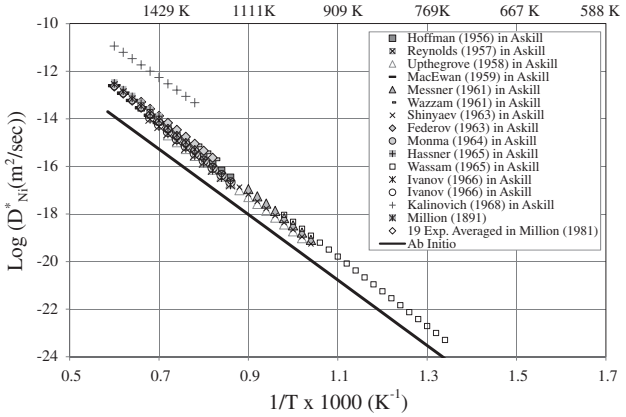

Fig. 1. Ni self-diffusion coefficients [22,24].

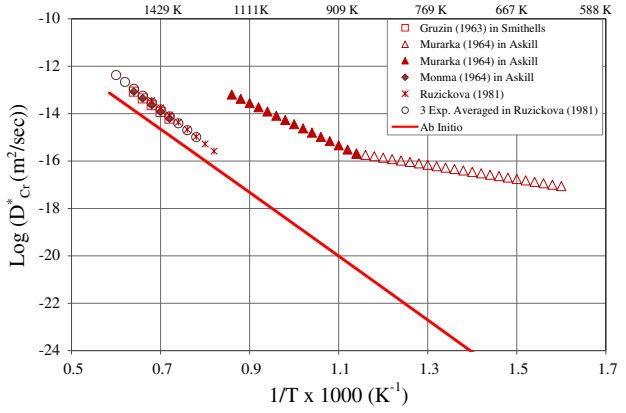

Fig. 2. Cr in Ni tracer diffusion coefficients [22,23,27].

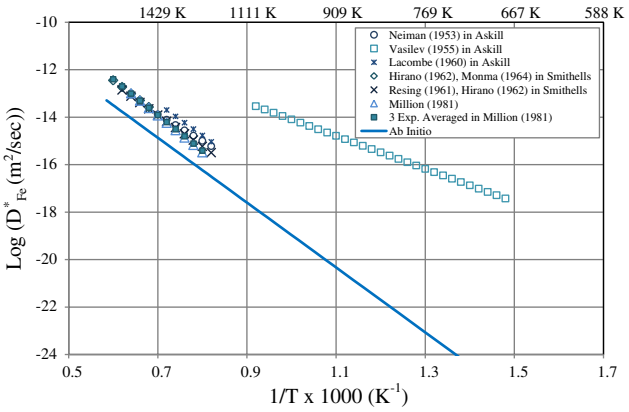

Fig. 3. Fe in Ni tracer diffusion coefficients [22–24].

diffusion coefficients may be partly attributed to the approximate treatment of vibrations in this work (in particular, the local vibrational model used and the neglecting of anharmonic vibrational contributions such as thermal expansion) and to contributions associated with magnetic excitations, which have not been included in the model (e.g., the ferromagnetic to paramagnetic transition in Ni). Approximations made to simplify many-electron interactions in *ab initio* methods also introduce error that is not easy to quantify.

It is likely that the disagreement between the experimental and calculated diffusion data comes from multiple sources. However, based on the data in Figs. 1–3 it appears that the largest difference between the *ab initio* and the experimental diffusion coefficients comes from the pre-exponential factor, since the calculated slopes for the three cases are in good agreement with most of the experimental data. In order to understand which variables could account for an order of magnitude disagreement, each variable in the Ni self-diffusion coefficient (see Eqs. (C.16)–(C.18)) has been varied independently until agreement with the experimental diffusion coefficient is reached. Table 2 presents a variable in the diffusion coefficient expression, its original *ab initio* value and the value required to account for the error in the Ni self-diffusion coefficient at 1650 K. For the purposes of this table, the experimental Ni self-diffusion coefficient is set to an average over 19 experiments [24] (shown in Fig. 1) and has a value of 1.81×10^{-13} m^2/s at 1650 K (the unaltered *ab initio* value is 9.80×10^{-15} m^2/s at 1650 K).

Here we consider the changes in each variable needed to match the experimental Ni diffusion values. The *ab initio* vacancy formation and migration enthalpies, H_{vf} and H_{mig}, are in good agreement with the experimental values of 1.79 eV and 1.04 eV [25], respectively. Furthermore, the altered values of the vacancy formation and migration enthalpies are significantly less than both experimental and *ab initio* values. In addition, the work of De Koning et al. [26] in Ni shows that the vacancy formation enthalpy is expected to increase with temperature, not decrease. Together these

Table 2
Ab initio values and adjusted values required to match *ab initio* and experimental Ni self-diffusion values.

Parameter	*Ab initio* value	Value needed to fit experiment
S_{vf} (k_B)	1.82	4.72
H_{vf} (eV)	1.65	1.24
H_{mig} (eV)	1.09	0.67
ν_{mig} (Hz)	4.48×10^{12}	8.25×10^{13}
Ni DOS (TS–OL) (states/eV/cell)	−0.66	11.80
EC_{mig}	0.86	15.80

results suggests that the vacancy formation and migration enthalpies are not a primary source of error in the diffusion coefficient calculations. The altered attempt frequency is above the typical phonon frequency range of 10^{12}–10^{13} and therefore seems unlikely to be a primary source of disagreement between the diffusion coefficients. The change needed in the Ni density of states (DOS) for the electronic migration contribution, EC_{mig}, seems unphysical as it is much larger than seen in any of the calculations. The altered value of the vacancy formation entropy, S_{vf}, is comparable with other values reported for Ni in Ref. [26], which are 3.3 k_B between 1200 and 1650 K from differential-dilatometry measurements and 5 k_B at the melting point, calculated from EAM potentials. The literature data suggests that the temperature dependence of vacancy formation entropy was not well represented by the classical high temperature approximation used in Eq. (D.1), and that this value is likely to be the main source of disagreement between the experimental and *ab initio* diffusion coefficients.

In order to provide the most accurate possible model for Ni, Fe and Cr diffusion in Ni, we use an empirical fit here to provide a small modification of the *ab initio*-based model. Based on the results in Table 2 and the above discussion, the disagreement between the calculated and experimental diffusion data can be largely attributed to errors in the temperature dependence of the Gibbs free energy of vacancy formation, G_{vf}, containing contributions from both S_{vf} and H_{vf}. To provide an optimized model a new high temperature G_{vf} is determined by using the experimental H_{vf} value and fitting S_{vf} to reproduce the averaged experimental diffusion data from Ref. [24] at 1650 K. Both S_{vf} and H_{vf} are assumed to be constant with temperature. The experimental H_{vf} value of 1.79 eV is now used because it was determined from measurements taken at finite temperatures and is more appropriate for high temperature fitting than the 0 K *ab initio* value. The value of S_{vf} determined from the fit is 5.71 k_B, which is different from the value in Table 2 due to the use of the experimental H_{vf} value.

In Fig. 4, the Ni, Fe and Cr calculated tracer diffusion coefficients, using both the *ab initio* and the new G_{vf} value with fitted S_{vf}, are compared to experimental tracer diffusion data. The *ab initio* diffusion coefficients use values from Table 1 only and the diffusion coefficients with the new G_{vf} use the same values from Table 1 but H_{vf} and S_{vf} are set to 1.79 eV and 5.71 k_B, respectively. The experimental values and their error bars in Fig. 4 are from Refs. [24,27] and are consistent of averages over multiple experimental data sets. Both sets of calculated diffusion coefficients capture the relative relationships between migrating species quite well. This suggests that the unaltered *ab initio* data could be used as is for studies involving relative behavior between diffusing species. Using the new G_{vf} value with fitted S_{vf}, improves the agreement with experiment to within the experimental error bars for all species. The values of H_{vf} and S_{vf} used to give the new G_{vf} are used here to provide an optimized model for the diffusion coefficients for practical applications, but are not used for any later calculations unless stated explicitly.

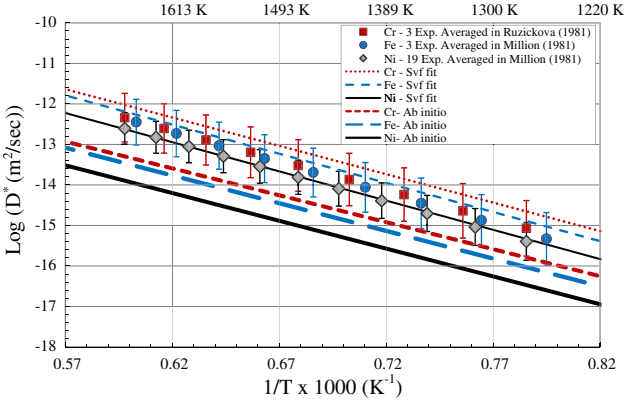

Fig. 4. *Ab initio* and averaged experimental Ni, Cr and Fe tracer diffusion coefficients in Ni [24,27].

Table 3 provides a comparison between the *ab initio* diffusion coefficients, with and without S_{vf} fitting, and the experimental diffusion coefficients by partitioning between the pre-exponential factor, D_0, and the activation energy, Q, defined in Eqs. (C.13), (C.14), (C.17), and (C.18). The *ab initio* pre-exponential factors are temperature dependent. In order to have a direct comparison with experimental data, Q and D_0 have been determined by fitting an Arrhenius equation to the *ab initio* diffusion predictions in the temperature range of 1250–1650 K. The order of the calculated activation energies is consistent with the ordering of the calculated diffusion coefficients in Fig. 4. In particular, Cr has a significantly lower migration barrier than Fe or Ni (0.83 eV compared to 0.97 eV or 1.09 eV, respectively, from Table 1), which drives faster diffusion. The identification of a low migration barrier as the source for fast Cr-vacancy mediated diffusion diverges from the interpretation of some previous authors who identified the pre-exponential factors as being the source of fast Cr diffusion [28]. It should be noted that the spread in experimental tracer diffusion coefficient data for Cr and Fe, as shown by error bars in Fig. 4, are relatively large and therefore it is possible that the experimentally derived ordering may change with further experimental work.

The temperature dependence of the pre-exponential factor, $D_0(T)$ of each species is illustrated in Fig. 5 using the unaltered *ab initio* diffusion coefficients data. The relative changes with temperature are the same for the S_{vf} fit data but using the unaltered data allows for a more straightforward comparison with the interstitial results, where experimental data is not available for fitting. The pre-exponential factor for solute diffusion has temperature dependent contributions from electronic excitations due to migration and binding (EC_{mig} and EC_{bind}) and from the correlation factor (f_2). In Fig. 5 the Ni pre-exponential factor varies mildly with temperature due to the fact that the electronic excitation contribution due to migration is the only temperature dependent variable in the pre-exponential factor. The electronic excitation contribution has a weak temperature dependence and varies only 20% from 100 to 1700 K. The pre-exponential factors for Cr and Fe exhibit strong temperature dependence, largely due to the correlation factor, which has a value near 0.5 at 1700 K and goes to zero at low

Table 3
Arrhenius fit of *ab initio* and experimental data averaged over 1250–1650 K.

Tracer species	D_0 (m^2/s) *ab initio* Arrhenius fit	D_0 (m^2/s) S_{vf} fit Arrhenius fit	D_0 (m^2/s) averaged exp. [24,27]		Q (eV) *ab initio* Arrhenius fit	Q (eV) S_{vf} fit Arrhenius fit	Q (eV) averaged exp. [24,27]
Ni	2.03×10^{-6}	1.00×10^{-4}	1.85×10^{-4}	$+0.76 \times 10^{-4}$ -0.53×10^{-4}	2.72	2.86	2.95 ± 0.08
Cr	4.52×10^{-6}	2.23×10^{-4}	2.26×10^{-4}	$+2.56 \times 10^{-4}$ -1.20×10^{-4}	2.64	2.78	2.89 ± 0.09
Fe	5.18×10^{-6}	2.56×10^{-4}	4.14×10^{-4}	$+4.0 \times 10^{-4}$ -2.0×10^{-4}	2.71	2.85	2.98 ± 0.09

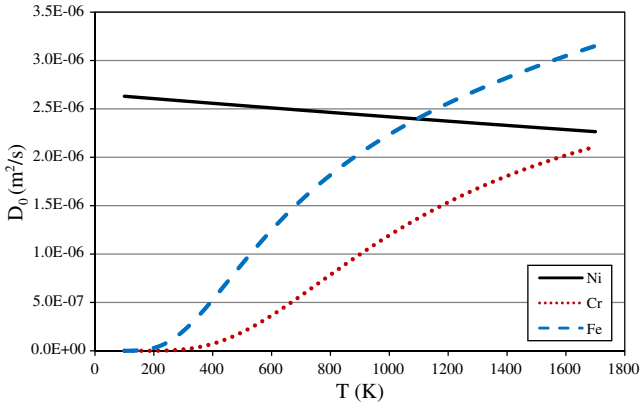

Fig. 5. Temperature dependence of the *ab initio* $D_0(T)$ for vacancy tracer diffusion.

temperature. This change in correlation factor is due to the fact that the vacancy–solute exchange hop has the lowest migration barrier for both alloys (as shown by $\Delta H_{mig} w_2$ in Table 1) and at low temperature the back and forth vacancy–solute exchange dominates and does not contribute to diffusion. The electronic contributions to $D_0(T)$ for Cr and Fe vary 10–20% over the temperature range studied and also contribute to the temperature dependence of the pre-exponential factor.

The temperature dependence of $D_0(T)$ is especially important when low temperature diffusion information is needed. For example, the temperature range 450–900 K is often of interest for studies of diffusion by radiation-induced defect concentrations [6]. The Arrhenius fit to experimental data typically does not account for the known physical temperature dependence of the pre-exponential factor. Arrhenius fits to experimental data that appear identical on log plots can have very different low temperature extrapolation due to the partitioning between D_0 and Q and the lack of temperature dependence in those values. To demonstrate the possible errors associated with using an Arrhenius fit to only high-temperature data we extrapolate Cr/Ni, Fe/Ni and Cr/Fe tracer diffusion coefficient ratios to low temperature for four cases (Fig. 6): (1) an experimental data set by Million [24] and Ruzickova [27], (2) an average of several similar experimental data sets [24,27], (3) the *ab initio* data fit with an Arrhenius equation at 1250–1650 K, and (4) the temperature dependent *ab initio* data. The difference between the Ruzickova/Million data and the averaged experimental data sets gives an indication of the disagreement within the existing experimental data, which is largely due to different partitioning between D_0 and Q in the diffusion coefficients. The difference between the *ab initio* sets indicates the error associated with the Arrhenius fit that lacks a temperature dependence pre-exponential factor. The difference between the Arrhenius fit *ab initio* data and the averaged experimental data indicates the error in the calculations and different partitioning of D_0 and Q. However, much of the error of the calculations cancels when the ratio is taken.

The experimental data sets in Fig. 6a have different trends due to the relative values assigned to Q_{Cr} and Q_{Ni}. The Arrhenius fit *ab initio* data would over predict the low temperature diffusion ratio but the temperature dependent D_0 suppresses this behavior. In Fig. 6b, both the *ab initio* and the experimental data sets agree fairly well at high temperature but have different low temperature trends due to the relative value of the activation energies. The *ab initio* curve has some non-Arrhenius behavior at low temperature, although it has a small quantitative effect over the temperatures considered. Fig. 6c shows good agreement for all data sets at high temperature. However, all sets over predict the temperature dependent *ab initio* values at low temperature, due to the Arrhenius fit.

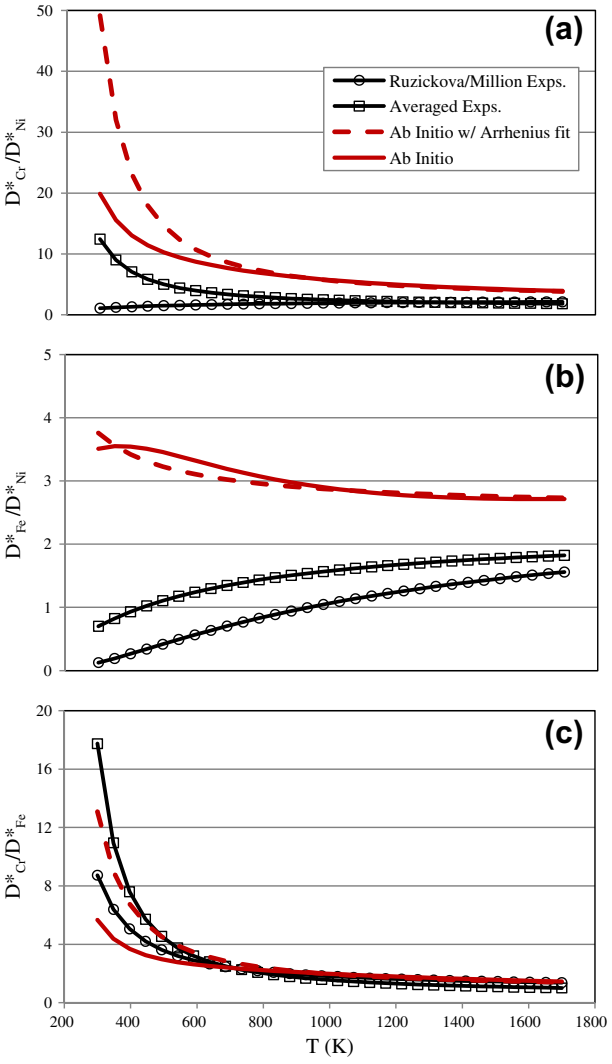

Fig. 6. Ratios of tracer diffusion coefficients: (a) Cr/Ni, (b) Fe/Ni, and (c) Cr/Fe with experimental data from Million et al. [24] and Ruzickova and Million [27].

The deviation from Arrhenius behavior of each species can be analyzed by taking the ratio of the *ab initio* diffusion coefficients fit to the Arrhenius form and the *ab initio* diffusion coefficients with the full temperature dependent pre-exponential factor. Fig. 7 shows this ratio for Ni, Cr and Fe tracer diffusion coefficients. Fig. 7 shows that Cr has the largest error associated with the Arrhenius fit, which explains the larger differences in the *ab initio* diffusion coefficient ratios containing Cr in Fig. 6a and c. For vacancy mediated diffusion in Ni, the Arrhenius fit is not a significant source of error. The error for Cr diffusion is near a factor of 2 at 450 K and the Fe and Ni errors are small. Significantly larger errors from high temperature Arrhenius fitting are found for interstitials and will be discussed in Section 3.2.

In addition to calculating diffusion coefficients, the values in Table 1 can be used to calculate the vacancy wind parameter, G. The vacancy wind parameter is a function of the phenomenological coefficients and determines the diffusion mechanisms present in dilute Ni–Cr and Ni–Fe alloys. The vacancy wind parameter is defined mathematically in Eqs. (C.19) and (C.20). When $G > -1$ it denotes that the vacancies and solute atoms are moving in opposite directions, which is expected from a simple exchange mechanism. When $G < -1$, it indicates that the drag mechanism is dominant and the vacancies and solutes are diffusing as a complex. This can occur when the rate of a vacancy to circle the solute is favored

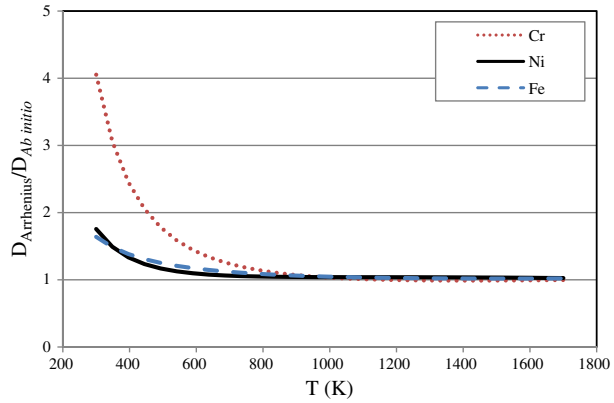

Fig. 7. Ratio of Arrhenius fit and *ab initio* diffusion coefficients for Ni, Cr and Fe diffusion coefficients for vacancy diffusion.

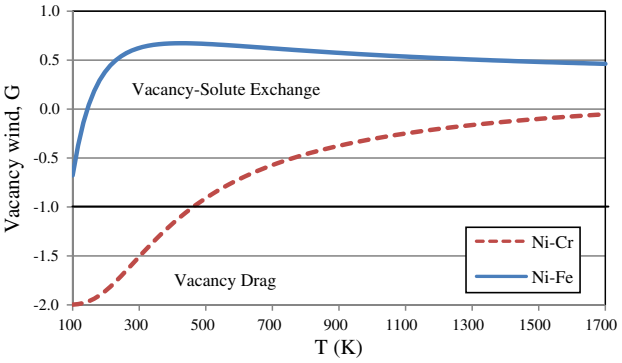

Fig. 8. Vacancy wind parameter, G for Ni–Cr and Ni–Fe.

over dissociation from the solute. The migration barriers for dissociation ($\Delta H_{mig} w_3$) and first nearest-neighbor (circling) hops ($\Delta H_{mig} w_1$) are provided in Table 1 for both the Ni–Cr and Ni–Fe system. Fig. 8 shows the vacancy wind parameter, G, as a function of temperature for Ni–Cr and Ni–Fe.

For Ni–Fe, the rate of dissociation is higher than the rate of circling the solute due to the migration barriers associated with these hops. Therefore, the drag mechanism will not be favorable at any temperature in this system. Fig. 8 confirms this and shows that G for Ni–Fe is always greater than -1. In the Ni–Cr system the migration barrier of circling the solute is lower than that of dissociation, which makes a mechanism change possible. Fig. 8 shows that G drops below -1 for Ni–Cr around 460 K. This means that at temperatures below 460 K the vacancy drag mechanism would be the dominant diffusion mechanism for the Ni–Cr system. Vacancy drag is generally associated with strong vacancy–solute binding, where the vacancy and solute move collectively due to the high energy cost of dissociation. However, in the case of Ni–Cr, the vacancy drag mechanism is due to the balance of the migration barriers and is not associated with vacancy–solute binding (in fact, the Cr-vacancy first nearest-neighbor interaction is about 50 meV and repulsive (Fig. D.1)).

3.2. Interstitial mediated diffusion

The tracer diffusion coefficients for interstitials can also be determined using *ab initio* methods. The *ab initio* data needed for modeling interstitial diffusion is given in Appendix D. We were not able to determine the value of the formation entropy, S_{If}, from *ab initio* methods (see Appendix D for details). However, interstitials can have large formation entropies, which have significant contributions to the diffusion coefficients, and need to be included in the diffusion expression. A value for S_{If} in Ni, determined by Debiaggi et al. [29] using an EAM potential, is available in the literature and will be used to calculate the diffusion coefficients. The interstitial tracer diffusion coefficients have been calculated using Eqs. (C.22) and (C.30) and the parameters summarized in Table 4. The tracer diffusion coefficients for Ni, Cr and Fe in Ni by an interstitial flux are shown in Fig. 9. Experimental data is not available for comparison with the calculated diffusion coefficients. The *ab initio* vacancy tracer diffusion coefficients (without S_{vf} fitting) are included in Fig. 9 for comparison in the temperature range of 1220–1700 K.

The order of the tracer diffusion coefficients are the same for the interstitials as for the vacancies, with Cr being the fastest diffuser,

Table 4
Parameters for interstitial mediated tracer diffusion in Ni.

Parameter	Value	Units
Ni parameters		
a	0.35239	nm
S_{If}[a]	12.7	k_B
H_{If}	4.07	eV
ν_{mig} Ni	4.48×10^{12}	Hz
Ni DOS (TS–OL)	−0.36	states/eV/cell
$\Delta H_{mig}\ w_0$	0.14	eV
$\Delta H_{mig}\ w_{R0}$	0.92	eV
Cr in Ni parameters		
ν_{mig} Cr	4.92×10^{12}	Hz
Cr DOS (TS–OL)	−0.77	states/eV/cell
H_{bind} Cr	−0.18	eV
ν_{bind} Cr	1.00	N/A
Cr DOS (OL–∞)	2.07	states/eV/cell
$\Delta H_{mig}\ w_1$	0.08	eV
$\Delta H_{mig}\ w_R$	0.75	eV
$\Delta H_{mig}\ w_2$	0.31	eV
$\Delta H_{mig}\ w_2'$	0.00	eV
$\Delta H_{mig}\ w_3$	0.26	eV
$\Delta H_{mig}\ w_4$	0.15	eV
Fe in Ni parameters		
ν_{mig} Fe	4.14×10^{12}	Hz
Fe DOS (TS–OL)	2.09	states/eV/cell
H_{bind} Fe	−0.01	eV
ν_{bind} Fe	1.00	N/A
Fe DOS (OL–∞)	−7.13	states/eV/cell
$\Delta H_{mig}\ w_1$	0.11	eV
$\Delta H_{mig}\ w_R$	0.87	eV
$\Delta H_{mig}\ w_2$	0.15	eV
$\Delta H_{mig}\ w_3'$	0.20	eV
$\Delta H_{mig}\ w_3$	0.14	eV
$\Delta H_{mig}\ w_4$	0.20	eV

[a] From Ref. [29].

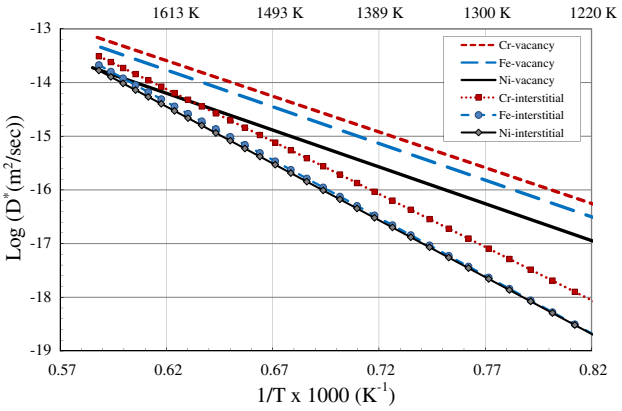

Fig. 9. *Ab initio* Ni, Cr and Fe interstitial and vacancy tracer diffusion in Ni.

then Fe, and then Ni. However, while Cr and Fe are quite close by the vacancy mechanism, Ni and Fe are quite close by the interstitial mechanism. The interstitial diffusion coefficients near the melting temperature are the same order of magnitude as the vacancy case, an effect that has been observed previously in Ref. [29]. However, the interstitial diffusion coefficients drop rapidly with temperature due to the large interstitial formation energy. The thermal concentration of interstitials is often assumed to be negligible due to their large formation enthalpy. However, dumbbell interstitials in fcc metals are known to have large formation entropies that can increase the thermal population. In some metals, the calculated concentrations of interstitials have been shown to rival divacancy concentrations at temperatures near the melting point [29]. The concentration of interstitials is still several orders of magnitude below the vacancy concentration at high temperature but the diffusion coefficients are similar due to the low migration barriers of the interstitials that enhance transport. Fig. 10 compares the calculated vacancy and interstitial concentrations as a function of temperature.

The ratios of the *ab initio* interstitial tracer diffusion constants (D_{Cr}/D_{Ni}, D_{Cr}/D_{Fe} and D_{Fe}/D_{Ni}) are shown in Fig. 11. The much faster diffusion of Cr is clear, with a tracer diffusion constant over 25 times that of Ni and 50 times that of Fe at 500 K. At high temperatures Fe is a faster diffuser than Ni but Ni becomes faster at 1180 K and below due to the temperature dependent pre-exponential factor of Fe, which decreases with decreasing temperature (see below for more discussion of this temperature dependence).

The interstitial diffusion coefficients have been fit with an Arrhenius equation over the temperature range of 1250–1650 K for comparison with the vacancy case and to assess the role of the pre-exponential factor and activation energy in the diffusion coefficient values. The values of the pre-exponential frequency factor and activation energy are given in Table 5 for both the vacancy and interstitial *ab initio* diffusion coefficients.

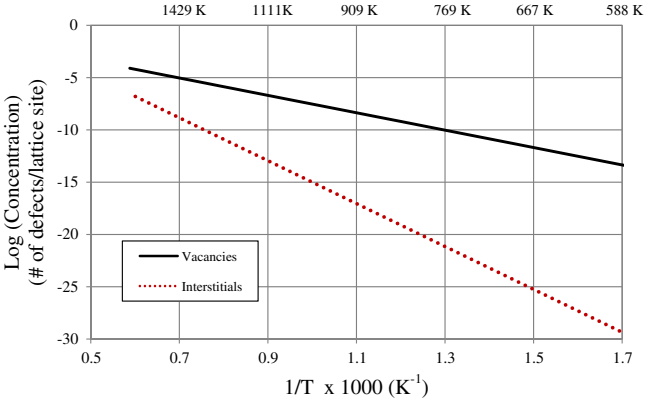

Fig. 10. Thermal concentrations of vacancies and interstitials.

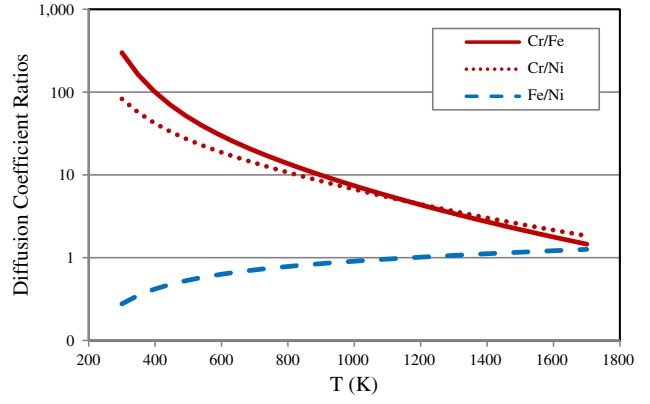

Fig. 11. Ratios of interstitial tracer diffusion coefficients Cr/Ni, Cr/Fe and Fe/Ni.

The ordering of Cr relative to Ni and Fe is due to the large difference in activation energy. The migration barriers of Ni and Cr in a Ni matrix only differ by 60 meV (w_0 and w_I in Table 4) but the large binding energy of Cr and a first nearest-neighbor *a*-type dumbbell (H_{bind} in Table 4) further reduces Cr interstitial activation energy by 180 meV, providing a large contribution to the overall 310 meV difference in the activation energies (see Table 5). The ordering of Ni and Fe depends largely on the pre-exponential factor since their activation energies are similar. While Fe has a larger pre-exponential factor in Table 5, it drops rapidly as a function of temperature due to the correlation factor and the electronic binding contributions. The temperature dependent pre-exponential factor of each species is shown in Fig. 12 and the contributing terms to this temperature dependence are shown in Fig. 13.

Comparing the vacancy diffusion data in Fig. 5 to that of the interstitials in Fig. 12 shows that the pre-exponential factor for interstitials is several orders of magnitude larger than that of vacancies. This can be attributed to the large formation entropy of interstitials, which appears in an exponential term in D_0. Similar to the vacancy case, the Ni–interstitial pre-exponential factor varies relatively little with temperature, due to the fact that the electronic migration contribution is the only temperature dependent variable in the pre-exponential factor and has weak temperature dependence. The pre-exponential factors for Cr and Fe vary dramatically with temperature because the correlation factors approach zero at low temperature (Fig. 13). As in the vacancy case, the back and forth hopping of the solute in the interstitial dominates at low temperature because the solute has a lower migration barrier than the Ni host (Cr and Fe $\Delta H_{mig} w_I$ in Table 4). Such back and forth hops do not contribute to long range diffusion and cause the correlation factor to go to zero at low temperatures.

The shape of D_0 for each species in Fig. 12 can be explained by the individual contributions of each temperature dependent variables in D_0, shown in Fig. 13. For Fe, there are strong temperature dependent contributions from the electronic excitation contributions to the binding energy and to a lesser extent, the correlation factor. These contributions are reflected in the pre-exponential factor in Fig. 12 by a steep increase with increasing temperature. In the case of Cr, the pre-exponential factor increases with increasing temperature until around 1100 K and then begins to decrease due to the electronic excitation contributions, which decrease with increasing temperature. The inversion of the D_0 curve is what leads to the low pre-exponential factor value for Cr in Table 5. For most contributions to D_0, a larger temperature dependence is observed for the interstitials than the vacancies. For interstitials, the contributions of electronic excitations to the interstitial binding energetics vary more with temperature than the other temperature dependent contributions for both Ni–Cr and Ni–Fe.

Similar to the vacancy case, the Arrhenius behavior of each species can be analyzed by taking the ratio of the *ab initio* diffusion coefficients fit to the Arrhenius form and the *ab initio* diffusion coefficients with the temperature dependent pre-exponential factor. The Arrhenius fit was performed over the temperature range of 1250–1650 K. Fig. 14 shows this ratio for Ni, Cr and Fe tracer diffusion coefficients and reveals that the Cr diffusion coefficient significantly deviates from Arrhenius behavior at low temperatures but the Fe and Ni diffusion coefficients are in good agreement with the Arrhenius fit. In the case of vacancies, the error in the Cr diffusion coefficient ratios introduced by the Arrhenius fit was approximately a factor of 2 at 450 K. For interstitials the error for Cr is a factor of 25 at 450 K, indicating strong non-Arrhenius behavior. For both vacancies and interstitials, cases involving Cr showed

Table 5
Ab initio pre-exponential factors and activation energy for interstitial and vacancy diffusion.

Tracer species	D_0 (m^2/s) interstitial Arrhenius fit	D_0 (m^2/s) vacancy Arrhenius fit	Q (eV) interstitial Arrhenius fit	Q (eV) vacancy Arrhenius fit
Cr	1.10×10^{-2}	4.52×10^{-6}	3.89	2.64
Fe	1.02×10^{-1}	5.18×10^{-6}	4.28	2.71
Ni	4.81×10^{-2}	2.03×10^{-6}	4.20	2.72

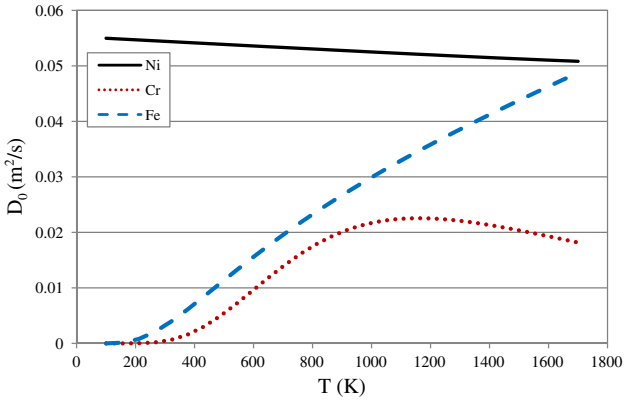

Fig. 12. Temperature dependence of the *ab initio* D_0 for interstitial tracer diffusion.

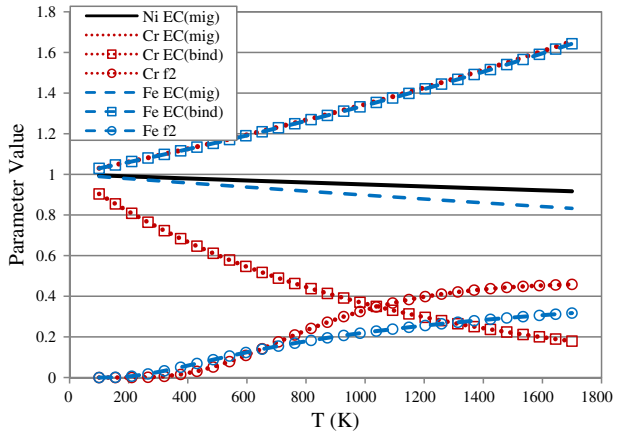

Fig. 13. Temperature dependent terms in D_0 for interstitial tracer diffusion.

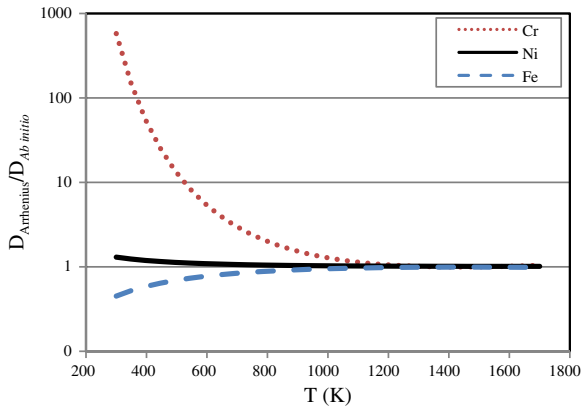

Fig. 14. Ratio of Arrhenius fit and *ab initio* diffusion coefficients for Ni, Cr and Fe diffusion coefficients for interstitial diffusion.

the largest errors, which implies that the diffusion of Cr through either defect has a non-Arrhenius temperature dependence.

For completeness we point out that, similar to the vacancy wind, one can define an interstitial wind, G_I, which determines relative direction of the solute and interstitial fluxes. The expression for G_I is given in Eq. (C.34). For the interstitial case, $G_I > -1$ means that the solute and interstitial fluxes are moving in the same direction and $G_I < -1$ means they are moving in opposite directions. Based on Eqs. (B.15) and (B.16) it is clear that within the model used in this work $G_I \geqslant 0$. This constraint yields $G_I > -1$, which implies that the solute moves with the interstitial flux, as expected.

3.3. Implications for radiation-induced segregation

Radiation-induced segregation (RIS) is a phenomenon that results in changes in the local composition near point defect sinks (i.e., grain boundaries) in irradiated alloys. RIS has been widely studied in both fcc Ni-based alloys and austenitic stainless steels [6] and bcc ferritic-martensitic Fe–Ni–Cr alloys [30]. RIS is caused by different diffusion rates of the major alloying elements (Ni, Cr, and Fe), potentially through both vacancy and interstitial mechanisms. RIS generally takes place in the approximate temperature range of $0.2–0.5T_{melt}$. At lower temperatures, there is limited mobility of point defects that mitigates RIS by enhanced recombination and at higher temperatures, deviations in local composition are eliminated by back diffusion of vacancies. Unfortunately, due to limited experimental data, it has been difficult to rigorously determine the mechanisms governing RIS and build accurate models. The *ab initio* results in this work provide valuable insights into the mechanisms of coupled solute and point defect diffusion in fcc based Ni–Cr–Fe alloys.

The RIS at grain boundaries in fcc steels generally consists of Cr depletion, Ni enrichment, and possible compensating Fe enrichment or depletion. Here we focus on the Cr depletion effect, as it is the most robust, well documented, and of particular interest due to possible associated changes in materials properties (e.g., grain boundary sensitization). Cr depletion in fcc steels is generally believed to be caused by a vacancy–solute exchange mechanism (inverse Kirkendall effect), in which vacancies moving to sinks swap preferentially with Cr, depleting Cr at the sinks. This vacancy-exchange mechanism underlies the influential models of Perks et al. [31,32], the similar model of Watanabe et al. [33], the extensive analysis of Simonen and Bruemmer [34], and the more atomistic-based model of Allen and Was [35]. However, competing models to explain RIS in Fe–Cr–Ni have proposed significant roles for other mechanisms. In particular, a number of authors have proposed mechanisms that involve interstitial contributions. Lam et al. [36,37] invoked Ni–interstitial binding as a key mechanism of RIS in Ni–Cr–Fe. Later, in an attempt to model RIS in Fe–15Cr–20Ni irradiated with electrons at low and high temperature, Watanabe et al. [38], concluded that the introduction of a Ni–interstitial binding energy and different vacancy migration energies at different temperatures were required to accurately predict the segregation. Nastar et al. [39] modeled RIS in Ni–Cr–Fe ternary alloys by including expressions for both vacancy and interstitial contributions. Nastar's model resulted in multiple possible self-consistent solutions due to the existence of many more unknown parameters

than equations. A final solution, which contained both vacancy and interstitial contributions, was determined by comparison to the RIS data. Faulkner [40,41] concluded that repulsive interactions between interstitials and oversized Cr drive Cr from the grain boundary, which would imply that RIS is entirely due to interstitials and a negative defect–solute interaction with Cr. Finally, it should be noted that thermal non-equilibrium segregation (TNES), a phenomenon closely related to RIS, finds Cr enrichment due to inverse Kirkendal contributions [34,42,43]. This has sometimes been explained in terms of strong Cr–vacancy drag, but such a model is not consistent with the weak Cr–vacancy interaction (see Fig. D.1) and vacancy drag results (see Fig. 8) found here.

The results of this work suggest that both vacancy and interstitial mechanisms could play a role in Cr depletion in Ni based Ni–Cr–Fe steels. The predicted vacancy mediated tracer diffusion coefficients show that Cr is a significantly faster diffuser than Ni (see Fig. 6), implying that vacancy mediated diffusion will deplete Cr from sinks by the inverse Kirkendall effect at higher temperatures. At lower temperatures, the vacancy contribution to Cr depletion would be expected to decrease, and eventually change toward enrichment, as the vacancy drag mechanism begins to dominate around 460 K (see Fig. 8). At low temperatures vacancy transport slows and RIS becomes increasingly dominated by interstitial contributions. The interstitial mediated tracer diffusion coefficients in this work also predict that Cr is a faster diffuser, implying that the interstitial diffusion mechanism will enrich Cr at sinks. Interstitial wind calculations confirm that the solute is expected to move with the interstitial flux. However, temperatures below 460 K are often not of interest for RIS experiments because the low defect mobility enhances mutual recombination and reduces the amount of segregation.

Thus, this work suggests that the vacancy and interstitial mechanisms are driving Cr diffusion in opposite directions. The magnitude of the tracer diffusion coefficient ratio D_{Cr}/D_{Ni} for vacancies and interstitials at 450 K are about 11 and 33, respectively, suggesting very strong RIS tendencies for both depletion and enrichment. The actual RIS observed could therefore be a balance between these two mechanisms. Atomistic modeling has recently been used to demonstrate a similar balance between vacancy- and interstitial mediated Cr RIS tendencies in bcc Fe–Cr alloys with dilute Cr [30]. The difference between Fe and Ni diffusion coefficients is small for both vacancy and interstitial mediated transport. At 450 K the magnitude of the tracer diffusion coefficient ratio D_{Fe}/D_{Ni} for vacancies and interstitials are about 3.5 and 0.5, respectively. Both ratios indicate Fe depletion at grain boundaries and sinks but the overall effect is smaller than for Cr, consistent with the greater RIS of Cr compared to Fe observed in experiments [3].

The larger value of D_{Cr}/D_{Ni} might suggest that the interstitial mechanism should play a dominant role, leading to Cr enrichment at sinks. However, a number of other factors that could affect RIS behavior must be considered. A particularly important factor is that the present work is only for dilute concentrations. The diffusion coefficients in this work do not account for solute–solute interactions so the diffusion coefficient ratios may not apply at higher solute concentrations. Other more subtle effects may also occur at higher solute composition. For example, additional calculations published elsewhere demonstrate that Cr–Cr dumbbells are 0.92 eV more stable than Ni–Ni dumbbells [44]. Thus Cr–Cr dumbbells could form traps for Cr, slowing its transport and providing opportunities for increased vacancy–interstitial recombination. Cr–Cr trapping effects are not present in the dilute model described in this work. Additionally, the diffusion coefficients in this work assume transport through isolated defects and do not account for the effect of defect clusters. It has been shown with molecular dynamics simulations in Fe [45] and Fe–Cr [46] that a large fraction of interstitials, and to a lesser extent vacancies, form in clusters of two or more defects. Interstitial clusters are reported to be quite mobile with activation energies on the order of mono-interstitials [45]. The effect of these clusters on RIS could be significant, depending on their coupling with solutes. Finally, other factors besides intrinsic bulk transport properties may impact the composition of the flux reaching the grain boundaries. For example, it is well known that edge dislocations will preferentially absorb interstitials [47,48]. Perhaps biased absorption of interstitials over vacancies at some defect sinks reduces the overall interstitial flux to grain boundaries, where RIS is typically measured.

In summary, the calculated tracer diffusion coefficient values in this work suggest the observed RIS at grain boundaries in Ni-based (and perhaps Fe-based) Ni–Cr–Fe alloys could involve a balance between two large and opposing RIS tendencies, with Cr depletion being driven by vacancy mediated diffusion and Cr enrichment being driven by interstitial mediated diffusion. The observed RIS may therefore be affected by additional factors that alter the balance between these two intrinsic bulk mechanisms, such as overall composition or the fraction of point vs. cluster defect diffusion, and the concentration and absorption bias of sinks in the alloy. In particular, the observed Cr depletion at grain boundaries suggests that Cr interstitials flux is reduced compared to the values predicted in our dilute solute model and that vacancies introduce the dominant species dependent point defect flux at the grain boundary.

4. Summary

In this paper, tracer diffusion coefficients were calculated for Ni, Cr and Fe in a Ni host. Both vacancy and interstitial mediated diffusion coefficients were determined with an *ab initio*-based approach that utilizes existing statistical mechanics models for calculating correlation effects. The vacancy tracer diffusion coefficients were compared to existing experimental tracer diffusion data. The *ab initio* diffusion coefficients were fit with an Arrhenius form to assess the impact of the temperature dependent pre-exponential factor for low temperature diffusion extrapolations.

New observations and findings for dilute Cr and Fe in Ni include:

(1) The calculated vacancy mediated tracer diffusion coefficients under-predicted the experimental tracer diffusion data but predicted the relative relationship between species well. The discrepancy between experimental and *ab initio* data was attributed to the temperature dependence of the vacancy formation free energy, G_{vf}, and in particular, the *ab initio* calculated entropy contribution to the free energy. It was shown that fitting the entropy of formation, S_{vf}, to the experimental Ni self-diffusion coefficient at 1650 K improved the agreement between experiment and calculated tracer diffusion coefficients for all species.

(2) Cr was found to be the fastest diffusing species followed by Fe and then Ni for both vacancy and interstitial mediated diffusion above 1250 K. The ordering of the species is mainly attributed to the activation energies, and Cr has the lowest activation energy for both vacancy and interstitial diffusion. The pre-exponential factors (D_0 values in the relationship $D = D_0 e^{-Q/kT}$) have an effect on ordering when the activation energies are similar, which is the case for Fe and Ni–interstitial diffusion.

(3) The Fe and Cr pre-exponential factors were found to be strongly temperature dependent for both vacancy and interstitial mediated diffusion due to the electronic excitation and correlation factor contributions to the diffusion coefficients. The electronic excitations due to binding, which are often neglected, proved to be significant in the interstitial

case, where the temperature dependence was more dramatic than the correlation factor.

(4) The calculation of the vacancy wind revealed that the vacancy drag mechanism is the dominant vacancy mediated diffusion mechanism in Ni–Cr below 460 K. Above 460 K for Ni–Cr and at all temperatures for Ni–Fe, vacancy–solute exchange is the dominant diffusion mechanism.

(5) The tracer diffusion coefficient of each species through interstitials, near the melting temperature, is comparable to the vacancy mediated diffusion coefficients. The concentration of thermal interstitials is a few orders of magnitude smaller than the vacancy concentration but the migration barriers are lower and compensate for the smaller number of interstitials present.

(6) The Arrhenius fit to the high-temperature diffusion coefficients introduced errors of up to a factor of 2 in the vacancy case and a factor of 25 in the interstitial case at 450 K. Cr had the largest errors indicating non-Arrhenius diffusion behavior through both interstitial and vacancy mediated diffusion. Errors of this magnitude introduced by the Arrhenius fit to high-temperature diffusion results would have a strong effect on RIS predictions at lower temperature.

(7) For the first time calculated diffusion coefficients suggest that Cr radiation-induced segregation in fcc Ni–Cr–Fe alloys may include competing tendencies for depletion by vacancies and enrichment by interstitials. The experimentally observed Cr depletion at grain boundaries suggests that the Cr bias of the interstitial flux is being reduced by composition or microstructure effects not included in the model.

Acknowledgements

The authors would like to acknowledge George Young, Frédéric Soisson and Jean-Louis Bocquet for helpful comments on early versions of the paper and Alain Barbu and Maylise Nastar for helpful discussions. This research was performed under appointment to the Naval Nuclear Propulsion Fellowship Program sponsored by Naval Reactors Division of the US Department of Energy (DOE). We gratefully acknowledge financial support from the DOE Nuclear Engineering Research Initiative Program (NERI), award number DE-FC07-06ID14747 and computing support from the National Science Foundation (NSF), National Center for Supercomputing Applications (NCSA), award number DMR060007.

Appendix A. Atomic hopping rates for diffusion

Beginning from the Eyring–Polanyi equation [11,12] one can derive the rate of a diffusive jump of an atom in a crystal lattice. The Eyring–Polanyi equation is given for the rate of an atomic hop in general form as:

$$w = \frac{1}{\tau} = \frac{k_B T}{h} \exp\left(\frac{-\Delta G}{k_B T}\right) \tag{A.1}$$

In Eq. (A.1), $1/\tau$ is the mean rate of hopping, ΔG is the Gibbs free energy of activation, k_B is Boltzmann's constant, T is temperature and h is Planck's constant.

Note that this equation is derived based on the assumption that the initial state is in equilibrium with the activated state. It also assumes that if an atom reaches the transition state of a diffusive jump, then it will complete the hop to the final state and will not fall back into the well from which it came. This assumption, which is common for transition state theory, will result in a rate that is an upper limit.

It is convenient to write the total Gibbs free energy as a summation of the Gibbs free energy for a reference state plus the contributions of excitations to that reference state [49]. The reference state has been selected to be $H_o(\sigma)$, the zero temperature enthalpy for atomic configuration σ, which is also the output of most *ab initio* codes. The reference state is selected to be a system that contains no temperature dependence, no vibrational contributions (even zero-point energy) and has a fixed reference magnetic order. The reference state can contain defects and solute species in any configuration. The Gibbs free energy of a specific configuration is the zero temperature enthalpy of that configuration plus any free energy added due to excitations of the system. The electronic, vibrational, and magnetic excitations will be modeled as a function of volume and therefore written as Helmholtz free energies, F. Rigorously, the excitation thermodynamics will depend on volume, or equivalently, pressure. However, since it is only differences between on lattice and transition state values that will contribute to the final hopping rates, it is likely that cancellation effects will cause the volume to have only a minor influence on the excitation energetics. Therefore, in order to keep the calculations practical, the volume dependent contributions to the excitations will not be included in this study. Furthermore, it is assumed that the relevant excitations are electronic, vibrational and magnetic. Within these approximations the Gibbs energy of the solid is written:

$$G(\sigma) = H_0(\sigma) + G_{excite}(\sigma) \approx H_0(\sigma) + F_{excite}(\sigma) \tag{A.2}$$

The σ notation is now dropped on the right hand side since all parameters that are configuration dependent will be determined for a specific configuration. Each contribution to the Gibbs free energy can be calculated with existing *ab initio* techniques. As mentioned above, H_o is a direct output of *ab initio* codes. F_{Elec} accounts for energy contributions due to thermal excitation of electron states. The Sommerfeld approximation [50] is used to calculate F_{Elec} by the following equation

$$F_{Elec} = E_{Elec} - \mathrm{TS}_{Elec} = -\frac{\pi^2}{6}(k_B T)^2 n(\varepsilon_F) \tag{A.3}$$

In Eq. (A.3), the term, $n(\varepsilon_F)$, is the density of states (DOS) at the Fermi energy and has units of number of states per unit energy. The Sommerfeld approximation is applicable when the density of states is temperature independent and nearly constant within $k_B T$ of the Fermi energy [51], although the latter constraint can be removed by integrating numerically with the full density of states. A more accurate self-consistent treatment of the electronic thermodynamics at finite temperature is relatively straightforward with modern electronic structure codes but would require a separate *ab initio* calculation for each temperature. Using such an approach in temperature dependent diffusion coefficient expressions requires fitting a function for interpolating the electronic contributions as a function of temperature and has not been attempted here.

The vibrational excitation contribution, F_{Vib}, accounts for the zero-point energy and the temperature dependence of the vibrational energy in the system. Vibrations in solids are commonly treated with the harmonic approximation, where the potential energy is expanded to second order in the displacements of the atoms from their equilibrium positions and higher-order terms are ignored. In the harmonic approximation the basic thermodynamic quantities for lattice vibrations can be expressed [52]:

$$\begin{aligned} F_{Vib} &= k_B T \sum_{m=\text{all modes}} \ln[2\sinh(x_m)] \\ &\approx k_B T \left(\ln \prod_{m=\text{all modes}} 2x_m + \sum_{m=\text{all modes}} \mathrm{O}\left(\frac{\theta_D}{T}\right) k_B \theta_D \right) \end{aligned} \tag{A.4}$$

where $x_m = \frac{h\nu_m}{2k_BT}$, θ_D is the Debye temperature and ν is the frequency in Hertz. The approximation on the right hand side is valid for higher temperatures, where $T > \theta_D$. Thermal expansion due to vibrations is zero in this purely harmonic approach.

The magnetic excitation contributions, F_{Mag}, accounts for changes in electron spins from the reference magnetic state due to temperature. In some cases the magnetic free energy can be approximated by a Heisenberg model, but this approximation is best when the spins behave as stable localized moments on each atom. It is not clear that the Heisenberg model applies in such Ni-based systems and further work is needed to develop a validated model for treating magnetic excitations in this system. Therefore, no magnetic contributions to the excitations are included in this work (although zero temperature spin polarized energetics are used for all the reference states).

By combining Eqs. (A.1)–(A.4), a practical rate expression for migration is obtained and presented in Eq. (A.5). The change in Gibbs free energy is the difference between configurations where the migrating atom is at the transition state (TS) and in the on lattice (OL) state adjacent to the TS. The difference between the TS and OL will be denoted *mig* for migration.

$$w = \frac{k_BT}{h}\exp\left(\frac{-\Delta G}{k_BT}\right) = \frac{k_BT}{h}\frac{\exp\left(\frac{-(H_0^{TS}+F_{Elec}^{TS}+F_{Vib}^{TS})}{k_BT}\right)}{\exp\left(\frac{-(H_0^{OL}+F_{Elec}^{OL}+F_{Vib}^{OL})}{k_BT}\right)} = \nu_{mig}\mathrm{EC}_{mig}\exp\left(\frac{-\Delta H_{mig}}{k_BT}\right) \tag{A.5}$$

Since H_o contains no temperature dependence or vibrational contributions and assumes a fixed magnetic order, the only contribution to the Gibbs free energy is the difference in enthalpy at the TS and OL. ΔH_{mig} is the zero temperature migration enthalpy.

The expressions ν_{mig} and EC_{mig} are derived from excitations at the OL and TS positions due to vibrational and electronic contributions, respectively. The electronic contribution reduces to the exponential of a term proportional to the difference between the electronic density of states for the TS and OL states.

$$\mathrm{EC}_{mig} = \frac{\exp\left(\frac{\pi^2}{6}(k_BT)n^{TS}(\varepsilon_F)\right)}{\exp\left(\frac{\pi^2}{6}(k_BT)n^{OL}(\varepsilon_F)\right)} = \exp\left(\frac{\pi^2k_BT}{6}\left(n^{TS}(\varepsilon_F) - n^{OL}(\varepsilon_F)\right)\right) \tag{A.6}$$

Applying the truncated high temperature expansion in Eq. (A.4), the ratio of the vibrational contributions can be written:

$$\nu_{mig} = \frac{k_BT}{h}\frac{\exp\left(-\ln\prod_{3N-1}x_m^{TS}\right)}{\exp\left(-\ln\prod_{3N}x_m^{OL}\right)} = \frac{\prod_{3N}\nu^{OL}}{\prod_{3N-1}\nu^{TS}} \tag{A.7}$$

where N is the number of atoms and $3N$ is the number of degrees of freedom. For solids, $3N$ is replaced by $3N-5$ to exclude translational and rotational degrees of freedom. The k_BT/h term from Eq. (A.5) is included in vibration contribution expression in Eq. (A.7) because it cancels in a convenient way when the vibrational contributions are evaluated.

Parameters needed to evaluate Eq. (A.5) for a given system include vibrational frequencies, electronic density of states and zero temperature enthalpies. The migration enthalpy term is generally the dominant term since the rate depends on it in an exponential manner and there is usually a significant energy barrier associated with diffusion events. The magnitudes of the other contributions are system dependent and will be examined in Appendix D for the Ni–Cr and Ni–Fe systems.

Appendix B. Calculating phenomenological coefficients from atomic rates

Phenomenological coefficients describe the mobility of atoms and are the link between migration rates and diffusion coefficients. Analytical expressions of phenomenological coefficients are available for some simple systems, such as dilute binary systems with short range interactions. These expressions can be calculated directly with various atomic rates and interactions that define the solute–defect thermokinetics (multi-frequency models). These multi-frequency models will be this used in this appendix to calculate of phenomenological coefficients for both vacancy and interstitial mediated diffusion in dilute fcc systems. The relationship between the phenomenological coefficients and the intrinsic diffusion coefficients for each species will also be given.

B.1. Vacancy phenomenological coefficients

The rates of various atom–vacancy exchanges relative to a solute atom are needed to obtain the phenomenological coefficients. The model used in this work for the vacancies in the fcc lattice requires five rates and is commonly known at the five-frequency model, originally developed by Lidiard and Le Claire [9,10,53]. The rates of the five-frequency model are used to calculate the phenomenological coefficient expression given by Allnatt [54]. It should be noted that other phenomenological coefficients expressions have been developed and are reviewed in Refs. [55,56].

Fig. B.1 illustrates the various diffusion events, where w_i is the rate associated with each event of the five-frequency model. The fifth hop, w_o, is not shown and is the hop of a vacancy in the pure solvent. The labels on the atoms in Fig. B.1 denote their nearest-neighbor distance from the solute.

The phenomenological coefficients expressions are given in

$$L_{AA} = \left(\frac{ns^2}{6k_BT}\right)\left[12c'_\nu(1-7c'_B)w_0 + c_pA_{AA}^{(0)} + c_pA_{AA}^{(1)}\right] \tag{B.1}$$

$$L_{AB} = L_{BA} = \left(\frac{ns^2}{6k_BT}\right)c_pA_{AB}^{(1)} \tag{B.2}$$

$$L_{BB} = \left(\frac{ns^2}{6k_BT}\right)\left[c_pw_2 + \frac{-2c_pw_2^2}{\Omega}\right] \tag{B.3}$$

where

$$A_{AA}^{(0)} = 4w_1 + 14w_3 \tag{B.4}$$

$$A_{AA}^{(1)} = \left[\frac{-2(3w_3-2w_1)^2 + 28w_3(1-F)(3w_3-2w_1)\left(\frac{w_0-w_4}{w_4}\right) - 14w_3(1-F)(2w_1+2w_2+7w_3)\left(\frac{w_0-w_4}{w_4}\right)^2}{\Omega}\right] \tag{B.5}$$

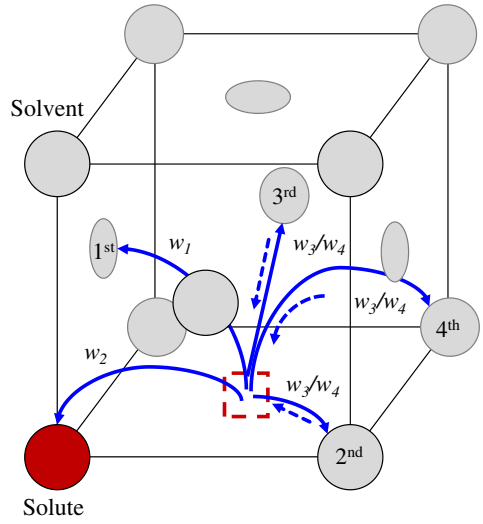

Fig. B.1. Illustration of five-frequency model.

$$A_{AB}^{(1)} = \frac{w_2\left[2(3w_3 - 2w_1) + 14w_3(1-F)\left(\frac{w_0 - w_4}{w_4}\right)\right]}{\Omega} \tag{B.6}$$

and

$$\Omega = 2w_1 + 2w_2 + 7w_3F \tag{B.7}$$

In addition to the five jump frequencies, there are a number of additional parameters that appear in Eqs. (B.1)–(B.3) and will be defined here. The number of lattice sites is denoted n, s is the nearest-neighbor jump distance ($s = a/\sqrt{2}$, where a is the lattice constant), c_p is the site fraction of solute atoms that have a vacancy among their nearest-neighbor sites (solute–vacancy pairs), c'_v is the site fraction of unbound vacancies (given by $c'_v = c_v - c_p$), and c'_B is the site fraction of unbound solutes (given by $c'_B = c_B - c_p$).

Eq. (B.8) is a mass-action equation that defines the relationship between the paired and unpaired vacancies and solutes. It is derived from the chemical potential, μ, relationship between secondary and primary species, $\mu_{Bv} = \mu_B + \mu_v$ and is a function of the coordination number, z, and the binding energy of the solute and vacancy, Δg_{Bv}. In the one-shell approximation of the five-frequency model the binding energy can be related to the ratio w_4/w_3 by detailed balance [55]. This approximation is only rigorously true when the vacancy and solute do not interact beyond the first shell and is therefore not recommended.

$$\frac{c_p}{c'_v c'_B} = z\exp\left(\frac{-\Delta g_{Bv}}{k_B T}\right) \tag{B.8}$$

The binding energy of a nearest-neighbor solute–vacancy pair is calculated using Eq. (B.9). Eq. (B.9) compares the energy of a configuration in which the vacancy and solute are first nearest-neighbors (nn) to configurations where the vacancy and solute are isolated or infinitely far apart (∞). When Δg_{Bv} is negative, there is an attraction between the solute and vacancy and the concentration of solute–vacancy pairs will be enhanced.

$$\Delta g_{Bv} = g_{B-v}^{1\text{st }nn} - g_{B-v}^{\infty} \tag{B.9}$$

The free vacancy concentration (site fraction) in pure solvent can be expressed in terms of the Gibbs free energy of formation at equilibrium (if the vacancy concentration is out of equilibrium, as for an irradiated system, then it must be obtained by other methods).

$$c'_v = \exp\left(\frac{-G_{vf}}{k_B T}\right) = \exp\left(\frac{-H_{vf}}{k_B T}\right)\exp\left(\frac{S_{vf}}{k_B}\right) \tag{B.10}$$

The enthalpy and entropy of formation are often known experimentally for pure materials or can be calculated. In pure materials the concentration of free vacancies and the total concentration of vacancies are equal, $c'_v = c_v$.

The factor F in Eq. (B.7) is a function of the ratio of w_4 and w_0 jumps as shown in

$$7(1-F) = \frac{10\xi^4 + B_1\xi^3 + B_2\xi^2 + B_3\xi}{2\xi^4 + B_4\xi^3 + B_5\xi^2 + B_6\xi + B_7} \tag{B.11}$$

where $\xi = w_4/w_0$.

The B_i coefficients have been determined using perturbation theory by Koiwa and Ishioka [57] and are given in Ref. [55].

With five rates, the binding energy of the solute–vacancy complex and the concentrations of vacancies and solutes, one can apply Eqs. (B.1)–(B.3) to calculate the phenomenological coefficients for any dilute fcc binary alloy. The necessary parameters for Ni–Fe and Ni–Cr alloys have been obtained in this work with *ab initio* methods and are given in Appendix D.

B.2. Interstitial phenomenological coefficients

The phenomenological coefficients for dumbbell interstitials in a dilute fcc system have been determined by Allnatt et al. [58] and Barbu [59] in the one-shell approximation that bears strong resemblance to the five-frequency model of the vacancy case. These expressions were derived under the assumption that the solute species is dilute enough to neglect solute–solute interactions. See Ref. [55] for a complete review.

The rates needed to determine the phenomenological coefficients are illustrated in Fig. B.2. The phenomenological coefficients are given in terms of the hopping rates by the following equation

$$L_{AA} = L_{AA}^f + L_{AA}^p \tag{B.12}$$

$$L_{AA}^f = \frac{4ns^2 c'_I w_0}{3k_B T} \tag{B.13}$$

$$L_{AA}^p = \left(\frac{ns^2 c_{pa} w_3}{6k_B T}\right)\left(-\frac{7w_0}{w_4} + \frac{16(w_3 + 2w_1 + w'_2)}{(5w_3 + 2w_1 + w'_2)} + \frac{12[(w_R + w_I)(2w_3 + w'_2) + 2w_3 w_2]}{[(w_R + w_I)(5w_3 + w'_2) + 5w_3 w_2]} + \frac{6w'_4(w'_3 + 2w'_1)}{w_4(2w'_3 + w'_1)}\right) \tag{B.14}$$

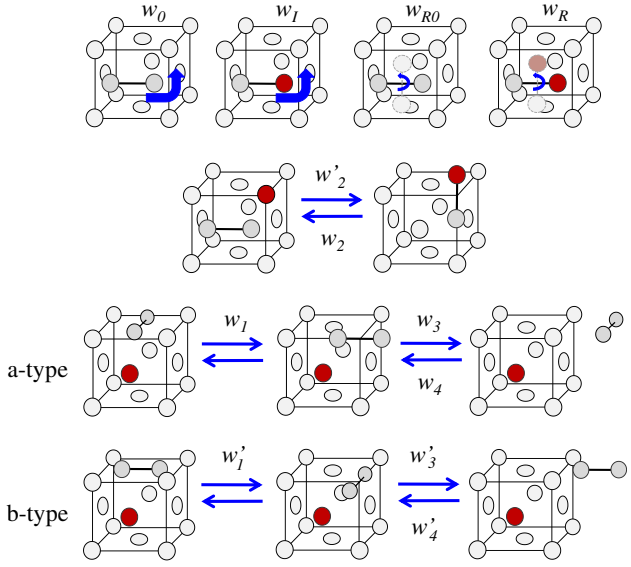

Fig. B.2. Illustration of different interstitial hopping events as defined by Barbu [59].

$$L_{AB} = L_{BA} = \left(\frac{ns^2 c_{pa}}{6k_B T}\right)\left(\frac{6w_I w_2' w_3}{A}\right) \tag{B.15}$$

$$L_{BB} = \left(\frac{ns^2 c_{pa}}{6k_B T}\right)\left(\frac{w_2' w_I}{w_2 A}\right)(w_R(5w_3 + w_2') + 5w_3 w_2) \tag{B.16}$$

where

$$A = (w_R + w_I)(5w_3 + w_2') + 5w_3 w_2 \tag{B.17}$$

c_{pa} is the site fraction of a-type solute–interstitial pairs (n_{pa}/n) and c_I' is the site fraction of unbound interstitials and c_B' is the site fraction of unbound solutes. The site fraction of b-type solutes does not contribute to the phenomenological coefficients directly since they are not oriented properly to become part of the interstitial dumbbell. The a- and b-type solute–interstitial pairs are shown in Fig. B.2. The total and bound solute and interstitial concentrations are related by $c_I' = c_I - c_{pa}$ and $c_B' = c_B - c_{pa}$. These concentrations are related by the following mass-action equation:

$$\frac{c_{pa}}{c_I' c_B'} = 8\exp\left(\frac{-\Delta g_{pa}}{k_B T}\right) \tag{B.18}$$

where Δg_{pa} is the binding energy of the solute–interstitial pair. The binding energy is taken by comparing the free energy of a system where the solute, B is an a-type nearest-neighbor of an A–A dumbbell interstitial (int) to a system where the solute and the A–A dumbbell are infinitely apart.

$$\Delta g_{pa} = g_{B-int}^{a\text{-type}} - g_{B-int}^{\infty} \tag{B.19}$$

The coefficient in front of the exponential in Eq. (B.18) coincides with the number of distinct configurations that lead to a c_{pa} pair. Only eight of the 12 nearest-neighbor sites of a dumbbell are a-type sites, the other four sites are orthogonal to the dumbbell axis and form b-type pairs.

The concentration (site fraction) of interstitials formed thermally in pure solvent is written using the same expression as for vacancies but now the enthalpy and entropy of formation are that of the dumbbell interstitial. In Eq. (B.20) it is implicitly assumed that there is only one interstitial configuration per lattice site. Additional configurations that are sampled at higher temperatures will appear as contributions to the entropy.

$$c_I' = \exp\left(\frac{-G_{If}}{k_B T}\right) = \exp\left(\frac{-H_{If}}{k_B T}\right)\exp\left(\frac{S_{If}}{k_B}\right) \tag{B.20}$$

B.3. Intrinsic diffusion coefficients

The phenomenological coefficients derived in Appendices A and B above contain the kinetic properties of the alloy and are closely related to the intrinsic diffusion coefficients. Diffusion coefficients are conveniently defined to allow one to describe the thermodynamic driving force in terms of gradients in concentration rather than gradients in chemical potential. This conversion allows for the flux of a species to be written in the conventional form of Fick's law where J_i is the flux, D_i is the intrinsic diffusion coefficient and n_i is the total number of atoms per unit volume of species i.

$$J_A = -D_A \nabla n_A; \quad J_B = -D_B \nabla n_B \tag{B.21}$$

The relationship between the intrinsic diffusion coefficients and the phenomenological coefficients is given in

$$D_A = \frac{k_B T}{n}\left(\frac{L_{AA}}{c_A} - \frac{L_{AB}}{c_B}\right)\left(1 + \frac{\partial \ln \gamma_A}{\partial \ln c_A}\right);$$
$$D_B = \frac{k_B T}{n}\left(\frac{L_{BB}}{c_B} - \frac{L_{BA}}{c_A}\right)\left(1 + \frac{\partial \ln \gamma_B}{\partial \ln c_B}\right) \tag{B.22}$$

In Eq. (B.22), γ_i is the activity coefficient of species i, c_i is the atomic fraction given by $c_i = n_i/n$, where n is the total number of atoms per unit volume. The second term in parenthesis is the thermodynamic factor that describes the change in chemical potential of one species with respect to the concentration of another species. The thermodynamic factor is equal to $\partial\mu_i/\partial c_j$ where the chemical potential is defined by $\mu_i = \mu_i^0(T,P) + k_B T \ln(c_i \gamma_i)$.

The expressions in Eq. (B.22) apply to both vacancy and interstitial mediated diffusion. The expressions can be further simplified in the dilute limit, where the thermodynamics factor is unity, in order to express the tracer diffusion coefficients in terms of the phenomenological coefficients. This derivation of the tracer diffusion coefficients is given in detail in Appendix C.

Appendix C. Tracer diffusion coefficients

Tracer diffusion coefficients can be determined for alloys with any concentration of solute species but the following discussion only applies to alloys with dilute solute concentrations (typically less than 1%). This appendix addresses binary alloys only but could also be applied to multi-component alloys where all of the solute concentrations are dilute and non-interacting. For example, the formulas in this appendix for binary tracer diffusion coefficients (D^*) can be applied to obtain D^* for Ni, Fe and Cr in Ni–Cr and Ni–Fe. These same D^* values will then also hold for ternary Ni–Fe–Cr in the limit of dilute Fe and Cr. Tracer diffusion coefficients of dilute species are determined by taking the limit of the intrinsic diffusion coefficients, defined in Appendix B, as the concentration of tracer species goes to 0. In the dilute limit, tracer diffusion coefficients offer an opportunity for experimental validation of the phenomenological coefficient expressions because the only factor that can lead to a net flow of tracer atoms is the concentration gradient of the tracer itself [60].

In this section, the tracer diffusion expressions are derived from the intrinsic diffusion coefficients and partitioned into pre-exponential frequency factors and activation energies to match the Arrhenius form of experimentally determined tracer diffusion coefficients.

C.1. Vacancy mediated diffusion

The tracer diffusion coefficient of solute B in the solvent A is determined by taking the limit of intrinsic diffusion coefficient, D_B, (Eq. (B.22)) as the concentration of species B goes to 0 (note that this will give $\gamma = 1$ in the dilute limit).

$$D_B^*(0) = \lim_{c_B \to 0} D_B = k_B T \frac{L_{BB}}{n_B} \tag{C.1}$$

To obtain the solute tracer diffusion coefficient, Eq. (B.8) for c_p is substituted into Eq. (B.3), which is used for L_{BB} in Eq. (C.1) to yield:

$$D_B^*(0) = \frac{s^2}{6} w_2 c_v' z \exp\left(\frac{-\Delta g_{Bv}}{k_B T}\right)\left[\frac{2w_1 + 7w_3 F}{2w_1 + 2w_2 + 7w_3 F}\right]$$
$$= a^2 w_2 c_v \exp\left(\frac{-\Delta g_{Bv}}{k_B T}\right) f_B \tag{C.2}$$

In the limit of $c_B \to 0$, $c_v' = c_v$, which is given by Eq. (B.10). The term in brackets in Eq. (C.2) is the correlation factor of the solute, f_B. The correlation factor is a measure of the extent to which the solute deviates from a perfect random walker. The correlation factor ranges from 0 to 1 where a perfect random walker has a value of unity.

$$f_B = \frac{2w_1 + 7w_3 F}{2w_1 + 2w_2 + 7w_3 F} \tag{C.3}$$

The binding energy is described in Eq. (B.9) as the change in free energy associated with bringing the solute and vacancy from a non-interacting position to a first nearest-neighbor position. Returning to the original definition of the Gibbs free energy, the binding energy can be described by the changes in the different contributions to the free energy, which can be written as:

$$\Delta g_{Bv} = \Delta H_0 + \Delta F_{Elec} + \Delta F_{Vib} \tag{C.4}$$

First, the change in zero temperature enthalpy simply compares the enthalpy of a configuration where the vacancy and solute are first nearest-neighbors (OL_2) to a configuration where they are considered infinitely far apart (∞). OL_2 denotes the on lattice position of the w_2 jump of the five-frequency model and ∞ denotes infinitely far apart or non-interacting. Note that, in general we will use OL_i and TS_i to refer to the state with the hopping atom in its on lattice or transition state position associated with hopping event i in Fig. B.1. The difference in enthalpy between these two configurations is the binding enthalpy and is given in

$$\Delta H_0 = H^{OL_2} - H^{\infty} = H_{bind} \tag{C.5}$$

Similarly, the electronic and vibrational contributions to the change in Gibbs free energy are found by subtracting the state where the vacancy and solute are non-interacting (∞) from the first nearest-neighbor position (OL_2).

$$\Delta F_{Elec} = -\frac{\pi^2}{6}(k_B T)^2 (n^{OL_2}(\varepsilon_F) - n^{\infty}(\varepsilon_F)) \tag{C.6}$$

$$\Delta F_{Vib} \approx k_B T \left(\ln \prod_{3N} \nu^{OL_2} - \ln \prod_{3N} \nu^{\infty} \right) \tag{C.7}$$

Now the binding energy contribution to $D_B^*(0)$ in Eq. (C.2) is written by combining Eqs. (C.4)–(C.7) to obtain:

$$\exp\left(\frac{-\Delta g_{Bv}}{k_B T}\right) = \exp\left(\frac{-\Delta H_0}{k_B T}\right) \exp\left(\frac{-\Delta F_{Elec}}{k_B T}\right) \exp\left(\frac{-\Delta F_{Vib}}{k_B T}\right) = \nu_{bind} \mathrm{EC}_{bind} \exp\left(\frac{-H_{bind}}{k_B T}\right) \tag{C.8}$$

where ν_{bind} is the vibrational contribution to binding given by Eq. (C.9) and EC_{bind} is the electronic excitation contribution to binding given by Eq. (C.10). Eqs. (C.9) and (C.10) are similar to those for EC_{bind} and ν_{bind} defined in Appendix A, except the infinitely far away position (∞) is evaluated instead of the TS position.

$$\nu_{bind} = \frac{\prod_{3N} \nu^{\infty}}{\prod_{3N} \nu^{OL}} \tag{C.9}$$

$$\mathrm{EC}_{bind} = \exp\left(\frac{\pi^2}{6} k_B T (n^{OL}(\varepsilon_F) - n^{\infty}(\varepsilon_F))\right) \tag{C.10}$$

All of the rates in the five-frequency model are needed to calculate $D_B^*(0)$. Each rate expression is obtained by inserting the corresponding TS and OL configuration into Eq. (A.5). For example, the rate expression for a solute–vacancy exchange, w_2, uses the OL_2 state (illustrated in Fig. B.1), where the solute and the vacancy are first nearest-neighbors, and the TS_2 state, which has the solute atom at the transition state.

$$w_2 = \nu_{mig}^{TS_2-OL_2} \mathrm{EC}_{mig}^{TS_2-OL_2} \exp\left(\frac{-\Delta H_{mig}^{TS_2-OL_2}}{k_B T}\right) \tag{C.11}$$

Here EC_{mig} and ν_{mig} are as defined in Eqs. (A.6) and (A.7), respectively. Eq. (C.11) is used to calculate the correlation factor in Eq. (C.3) and is applied directly in Eq. (C.2) to calculate $D_B^*(0)$. All of the terms needed to determine the tracer diffusion coefficient of the solute B, $D_B^*(0)$, in Eq. (C.2) have been defined in Eqs. (B.10), (C.3), (C.8), and (C.11). It is helpful to partition terms between the pre-exponential factor and activation energy to express the solute tracer diffusion coefficient in the Arrhenius form of

$$D_B^*(0) = D_{0A}^B \exp\left(\frac{-Q_A^B}{k_B T}\right) \tag{C.12}$$

where D_{0A}^B is the pre-exponential factor and Q_A^B is the activation energy, given by

$$D_{0A}^B = a^2 f_B \nu_{bind} \mathrm{EC}_{bind} \nu_{mig}^{TS_2-OL_2} \mathrm{EC}_{mig}^{TS_2-OL_2} \exp\left(\frac{S_{vf}}{k_B}\right) \tag{C.13}$$

$$Q_A^B = \Delta H_{mig}^{TS_2-OL_2} + H_{vf} + H_{bind} \tag{C.14}$$

The activation energy contains the migration and formation enthalpy of the vacancy and a binding enthalpy of the solute. The pre-exponential factor contains the correlation factor and many contributions associated with migration and binding, some of which are temperature dependent and cannot be easily resolved experimentally.

It is often useful to know the self-diffusion coefficient of a species. For pure A the self-diffusion coefficient is also a tracer diffusion coefficient for a species B but now species B is considered an isotope of species A. The self-diffusion coefficient of A can be determined from Eq. (C.2) by setting all of the jump rates equal to w_0 and $\Delta g_{Bv} = 0$. Note that $7F = 5.15$ for a w_4/w_0 ratio of unity. The self-diffusion coefficient can be written as:

$$D_A^*(0) = 2s^2 w_0 c_v \left[1 - \frac{2}{9.15}\right] = a^2 w_0 c_v f_0 \tag{C.15}$$

Again, the term in brackets is the correlation factor, f_0. For pure fcc metals, $f_0 = 0.7815$ [55].

Applying the rate definition in Eq. (A.5) to w_0, the full self-diffusion coefficient expression is obtained. The self-diffusion coefficient can be partitioned into the Arrhenius form of

$$D_A^*(0) = D_{0A}^A \exp\left(\frac{-Q_A^A}{k_B T}\right) \tag{C.16}$$

where

$$D_{0A}^A = a^2 f_0 \nu_{mig}^{TS_0-OL_0} \mathrm{EC}_{mig}^{TS_0-OL_0} \exp\left(\frac{S_{vf}}{k_B}\right) \tag{C.17}$$

$$Q_A^A = \Delta H_{mig}^{TS_0-OL_0} + H_{vf} \tag{C.18}$$

While the tracer diffusion coefficients provide essential information about A and B atom kinetics, they do not describe the kinetic cross terms between A and B and vacancies. A quantity of interest that does describe some of these cross term couplings is L_{vB}, which is useful for studying the relationship between the solute and the vacancy mobilities. L_{vB} is defined in terms of the phenomenological coefficients L_{AB} and L_{BB}.

$$L_{vB} = -(L_{AB} + L_{BB}) = -L_{BB}(G + 1) \tag{C.19}$$

where

$$G = \frac{L_{AB}}{L_{BB}} = \frac{-2w_1 + 3w_3 + 7w_3(1-F)\left(\frac{w_0 - w_4}{w_4}\right)}{w_1 + 3.5 w_3 F} \tag{C.20}$$

G is called the *vacancy wind* and accounts for the coupling between the flux of species A and B, J_A and J_B, through the vacancy flux, J_v [56]. It can be seen from Eq. (C.19) that if $G < -1$, then the sign of L_{vB} changes. A sign change denotes a change in the relative direction of solutes and vacancy.

In the five-frequency model the w_1 jump is one where the vacancy moves from one first nearest-neighbor position to another,

relative to the solute. The w_3 jump is the rate of dissociation between the solute and vacancy. In the fcc crystal structure it is possible for a vacancy to circle around the solute through a series of w_1 jumps without dissociation. If the rate of circling around the solute is much greater than the rate of dissociation it is possible to have a cooperative motion between the solute and the vacancy where they are traveling in the same direction. This mechanism is commonly referred to as the vacancy–solute drag mechanism. If L_{vB} is negative ($G > -1$), it indicates the solute and vacancy are moving in opposite directions, if positive ($G < -1$), it indicates that the drag mechanism is dominant and the vacancies and solutes are moving in the same direction. Note that the diffusion mechanism can change as a function of temperature since the rates are temperature dependent. The vacancy wind has been calculated for the Ni–Cr and Ni–Fe binaries as a function of temperature and the results are presented and discussed in Section 3.1 of the main text.

C.2. Interstitial mediated diffusion

The interstitial tracer diffusion coefficient is obtained by taking the limit of D_B from Eq. (B.22) as $c_B \to 0$, as in the vacancy case. In this case the phenomenological coefficients in Eq. (B.22) refer to those of the interstitial model in Eqs. (B.12)–(B.16).

$$D_B^l(0) = \lim_{c_B \to 0} D_B = k_B T \frac{L_{BB}}{n_B} \tag{C.21}$$

Inserting Eq. (B.16) for L_{BB} and Eq. (B.18) for c_{pa} results a tracer diffusion expression given by the following equation:

$$D_B^l(0) = \frac{2}{3} a^2 c_I \exp\left(\frac{-\Delta g_{pa}}{k_B T}\right) w_1 f_B \tag{C.22}$$

where c_I is the total concentration of interstitials (site fraction) and $c_I = c_I'$ in this limit. The correlation factor, f_B, is given by:

$$f_B = \frac{w_2'(w_R(5w_3 + w_2') + 5w_3 w_2)}{w_2((w_R + w_1)(5w_3 + w_2') + 5w_3 w_2)} \tag{C.23}$$

The definitions of the migration rates of interstitials have the same form as in the vacancy case. The activated state and the adjacent pre-hop configuration are now that of the interstitial dumbbell (illustrated in Fig. C.1a). The rate of dumbbell rotation is also needed to obtain the phenomenological coefficients. Assuming rotation in the {1 0 0} family of planes, the OL and TS states for rotation are shown in Fig. C.1b.

The rate of each event is determined by using the appropriate TS and OL configuration energetics in Eq. (A.5). The change in enthalpy for rotation is denoted *rot*. Eqs. (C.24) and (C.25) provide examples for the rates in Fig. C.1.

$$w_0 = \nu_{mig}^{TS_0 - OL_0} \mathrm{EC}_{mig}^{TS_0 - OL_0} \exp\left(\frac{-\Delta H_{mig}^{TS_0 - OL_0}}{k_B T}\right) \tag{C.24}$$

$$w_{R0} = \nu_{mig}^{TS_{R0} - OL_{R0}} \mathrm{EC}_{mig}^{TS_{R0} - OL_{R0}} \exp\left(\frac{-\Delta H_{rot}^{TS_{R0} - OL_{R0}}}{k_B T}\right) \tag{C.25}$$

Like the vacancy case, the binding energy is calculated by comparing the free energy change between the solute and dumbbell as

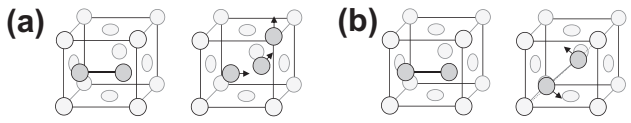

Fig. C.1. (a) OL_0 and TS_0 states for an interstitial migration event in pure solvent and (b) OL_{R0} and TS_{R0} for a w_{R0} type interstitial rotation event in pure solvent.

a-type first nearest-neighbors and infinitely far apart, as shown in Eq. (B.19).

$$\Delta g_{pa} = \Delta H_0 + \Delta F_{Elec} + \Delta F_{Vib} \tag{C.26}$$

$$\exp\left(\frac{-\Delta g_{pa}}{k_B T}\right) = \nu_{bind} \mathrm{EC}_{bind} \exp\left(\frac{-H_{bind}}{k_B T}\right) \tag{C.27}$$

Each term in the interstitial tracer diffusion coefficient expression in Eq. (C.22) has been defined and can now be partitioned into Arrhenius form with a pre-exponential factor, D_{0A}^B and activation energy, Q_A^B.

$$D_{0A}^B = \frac{2}{3} a^2 f_B \nu_{bind} \mathrm{EC}_{bind} \nu_{mig}^{TS_I - OL_I} \mathrm{EC}_{mig}^{TS_I - OL_I} \exp\left(\frac{S_{If}}{k_B}\right) \tag{C.28}$$

$$Q_A^B = \Delta H_{mig}^{TS_I - OL_I} + H_{If} + H_{bind} \tag{C.29}$$

The expression for the interstitial solute tracer diffusion coefficient is identical to that of the vacancy solute tracer diffusion coefficient except for the factor of 2/3 in front. The factor of 2/3 comes from the fact that there are eight nearest-neighbors oriented properly for diffusion (*a*-type) out of the total 12 nearest-neighbors. The coupling of neighbors and diffusion reduces the diffusion constant by 8/12 = 2/3.

To obtain the interstitial self-diffusion coefficient, the solute *B* is treated as an isotope of species *A*. In Eq. (C.22), we set $\Delta g_{pa} = 0$ and all rates to their pure solvent values, w_0 and w_{R0}. The self-diffusion coefficient becomes:

$$D_A^l(0) = \frac{2}{3} a^2 c_I w_0 f_0 \tag{C.30}$$

where

$$f_0 = \frac{6w_{R0} + 5w_0}{6w_{R0} + 11w_0} \tag{C.31}$$

and w_{R0} and w_0 are given in Eqs. (C.24) and (C.25).

The interstitial tracer self-diffusion coefficient expression partitioned into Arrhenius form yields a pre-exponential factor, D_{0A}^A and activation energy, Q_A^A, with expressions:

$$D_{0A}^A = \frac{2}{3} a^2 f_0 \nu_{mig}^{TS_0 - OL_0} \mathrm{EC}_{mig}^{TS_0 - OL_0} \exp\left(\frac{S_{If}}{k_B}\right) \tag{C.32}$$

$$Q_A^A = \Delta H_{mig}^{TS_0 - OL_0} + H_{If} \tag{C.33}$$

Again, the expression for interstitial self-diffusion coefficient is identical to that of the vacancy self-diffusion coefficient except for the factor of 2/3.

Similar to the case of vacancy, we can define an interstitial wind G_I by the relations:

$$L_{IB} = L_{AB} + L_{BB} = L_{BB}(G_I + 1); \quad G_I = \frac{L_{AB}}{L_{BB}} \tag{C.34}$$

For the vacancy case $G < -1$ ($L_{vB} > 0$) implies that the vacancy will drag the solute along with it. For the interstitial case, it is also useful to consider the region of G_I near -1. $G_I > -1$ ($L_{IB} > 0$) implies that the solute moves with the interstitial flux and $G_I < -1$ ($L_{IB} < 0$) implies that the solute moves opposite the interstitial flux. It is this latter case that would be considered unusual, analogous to the occurrence of vacancy drag, as the solute would be moving opposite the direction expected for a single component system with interstitial mediated transport. Based on Eqs. (B.15) and (B.16) it can be seen that, within the models used in this work, $G_I \geqslant 0$ and the solutes flux will be in the same direction as the interstitial flux.

Appendix D. Thermokinetic data obtained by first principles

Each contribution to the diffusion equation expressions (except where stated explicitly) is calculated using *ab initio* methods. However, there are 17 different hop types for the multi-frequency models being applied here (see Figs. B.1 and B.2 for hop types). In order to keep the number of calculations practical and consistent with the multi-frequency models, a few approximations must be made. For each hop the barrier is calculated explicitly. However, only approximate contributions from the excitations will be included. The primary approximation is to assume that the excitations are dependent on the hopping species only and independent of local configuration. This approximation implies that in calculating the Ni–Cr or Ni–Fe vacancy tracer diffusion coefficients, any Ni hop will be treated as a w_0-type Ni hop for all contributions except the migration barriers. For example, the vibrational frequencies at TS_1 and TS_3 are all assumed to be equal to TS_0. Recall that OL_i and TS_i refer to the state with the hopping atom in its on lattice or transition state position associated with hopping event i in Fig. B.1. The migration barrier will make up the dominant contribution for differences in hopping rates and the migrating species type should capture the main effect of the excitations. The states that are treated explicitly for all excitations, i.e., for which the excitation contributions are calculated from *ab initio* methods, are the TS_0, TS_2, OL_0, OL_2 and OL_∞ states for Ni–Cr or Ni–Fe. All other states are treated as equivalent to one of the states that are treated explicitly, as discussed above. The OL_2 and OL_∞ states are needed to calculate the binding energies of vacancies and solutes (the ∞ state refers to the case where the vacancy and solute are infinitely far apart).

For interstitial diffusion, an analogous approximation to that of the vacancy case would be to consider the excitations of every Ni hop as a w_0 hop for the interstitials. Again, the migration barriers for each type of hop are treated explicitly since they will make the largest contribution to the rate expression. The explicit treatment of excitations associated with dumbbell rotations are neglected because, as will be seen later, the rotation barrier is prohibitively high compared to the other possible events. This high barrier drives the rate of rotation events to zero and any contribution from excitations would become insignificant. The TS state of a Ni–Ni rotation is treated as a w_0 hop and a Ni–Cr/Fe rotation as a w_1 Cr or Fe hop. The states that will be treated explicitly for all excitations are the TS_0, TS_1, OL_0, OL_1, $OL_{2'}$ and OL_∞ states for Ni–Cr or Ni–Fe. The $OL_{2'}$ and OL_∞ states are needed to calculate the binding energies of a-type dumbbells.

D.1. Lattice parameter

The lattice parameter for pure Ni has been experimentally measured at room temperature to be 0.35238 nm [25] and 0.35157 nm at 50 K [61]. The *ab initio* calculated value in this work is 0.35239 nm, which is considered to be at 0 K. Since the models are appropriate when there is only a dilute amount of solute present (~1% or less), the pure Ni lattice constant is used for all tracer diffusion calculations. The *ab initio* calculated lattice parameter value will be used in order to be consistent with the other *ab initio* determined values.

D.2. Electronic contributions

In order to determine the electronic contributions, F_{Elec}, in Eq. (A.3), the density of states at the Fermi energy is needed for each configuration. Table D.1 displays the density of states (DOS) at the Fermi energy, $n(\varepsilon_F)$, for pure Ni and solute cases at the TS, OL and ∞ state for both interstitials and vacancies. The OL state has a solute atom as a first nearest-neighbor to a vacancy or an a-type first nearest-neighbor to an interstitial dumbbell. In the case of pure Ni, the OL and ∞ states are indistinguishable from each other. The DOS difference is taken and to calculate the electronic contribution associated with migration and binding. Recall that the DOS at the Fermi energy, $n(\varepsilon_F)$ is related to EC_{mig} and EC_{bind} as stated in Eqs. (A.6) and (C.10). EC_{mig} and EC_{bind} are temperature dependent quantities and their impact on the hopping rate can be significant. The electronic excitation contributions due to migration and binding will be included in the rate expression as a function of temperature.

Table D.1
DOS (number states/eV per cell) for electronic contribution to the rate equation.

Material	DOS (TS)	DOS (OL)	DOS (∞)	DOS (TS–OL)	DOS (OL–∞)
^{107}Ni + v	198.64	199.30	199.30	−0.66	0.00
^{106}Ni^{1}Fe + v	196.15	195.55	194.78	0.61	0.76
^{106}Ni^{1}Cr + v	200.93	201.36	200.93	−0.43	0.44
^{109}Ni *w/int*	209.15	209.51	209.51	−0.36	0.00
^{108}Ni^{1}Fe *w/int*	206.09	206.85	204.79	−0.77	2.07
^{108}Ni^{1}Cr *w/int*	206.88	204.79	211.92	2.09	−7.13

D.3. Vibrational contributions

The vibrational contributions of migration have been calculated using a local harmonic approximation [62]. A Hessian matrix is constructed and diagonalized to obtain frequencies, ν_j, for the OL and TS configurations. For a complete model the full dynamical matrix should be determined for the different states. However, an approximation that treats only the atom directly involved in the relevant processes is used here. For vacancies a single atom is displaced 0.001 nm along each of the Cartesian coordinates to determine the second derivatives of energy with respect to atomic position. In the OL state, a Ni or solute atom as a first nearest-neighbor to a vacancy is displaced. At the transition state, the hopping atom is displaced. The TS has one negative eigenvalue of the Hessian matrix, corresponding to an imaginary frequency. The ratio of the products of the real frequencies at the OL and TS are used to determine the vibrational migration contribution, also known as the attempt frequency, which was given in Eq. (A.7) (where N is the number of atoms displaced, which is one in this case).

This approach of treating vibrations locally has often been used for the diffusion of light atoms in a matrix of heavier atoms [63–65], where the mass difference helps make the local approach accurate. This method is used in this work to provide only approximate attempt frequencies since Ni, Cr and Fe are of similar mass. The attempt frequencies of vacancy–atom exchange for Ni, Cr and Fe migrating in a Ni host are calculated to be 4.48, 4.92 and 4.14 THz, respectively. These values are summarized in Table 1.

For the interstitial dumbbell migration, it was not possible to obtain an imaginary frequency at the TS by displacing a single atom. This is due to the fact that the dumbbell hop is a cooperative motion between three atoms and many more are displaced in the process. Therefore, an analogous equation to (A.7) for the attempt frequency for interstitials has not been constructed and instead the interstitial attempt frequencies are estimated as follows. Compared to the vacancy hopping, the interstitial migration barriers are lower and the distances traveled during a migration event are shorter. These two effects contribute opposite changes in the curvature of the energy surface as compared to a vacancy. Therefore, as a first approximation, the attempt frequencies to hop a given species by the vacancy mechanism will be used for the interstitial attempt frequencies for that species as well.

The vibrational contributions due to binding, ν_{bind}, are also calculated using the local harmonic approximation, Eq. (C.9). A single atom is displaced along each of the Cartesian coordinates to determine the second derivative of energy with respect to atomic positions. The values are determined by comparing the frequencies of a solute atom as a first nearest-neighbor to the defect and in pure solvent with no defect present (to simulate the ∞ state). Values of ν_{bind} are unitless because both states are normal lattice sites, not transition states, and they have the same number of frequencies. The values for Cr and Fe solutes next to a vacancy in Ni are 1.25 and 1.29, respectively. The vibrational contributions due to binding for the interstitial dumbbells were not calculated due to problems obtaining converged values, which seemed to require a very large number of atoms around the interstitial. A value of unity is used for vibrational contributions to interstitial binding in the diffusion coefficient calculations. The vacancy and interstitial values of ν_{bind} are summarized in Tables 1 and 4, respectively.

D.4. Defect concentration parameters

In order to calculate the concentration of thermally created interstitial and vacancy defects the entropy and enthalpy of formation must be determined. The entropy of formation for a single vacancy or interstitial can be expressed in the harmonic approximation by:

$$S_i^f = k_B \sum_{\alpha=1}^{3N} \ln\left(\frac{\nu_\alpha^0}{\nu_\alpha}\right) = k_B \ln\left(\frac{\prod_{\alpha=1}^{3N} \nu_\alpha^0}{\prod_{\alpha=1}^{3N} \nu_\alpha}\right) \tag{D.1}$$

where ν_α^o are the eigenfrequencies of the ideal lattice and ν_α are those of the defected lattice. Note that Eq. (D.1) is the classical high temperature limit but is applied to zero temperature defect calculation following standard practices [29,66]. Eq. (D.1) is generally assumed to be accurate for the Debye temperature and above. The *ab initio* result for the vacancy formation entropy is 1.82 k_B, which is converged for temperatures above 100 K in the classical high temperature limit. The interstitial formation entropy was not calculated in this work but a value has been previously reported in the literature. Debiaggi et al. [29] have calculated the formation entropy of a ⟨1 0 0⟩ type interstitial in pure Ni at 0 K to be 12.7 k_B using EAM potentials and the harmonic approximation. This value will be used in the calculation of interstitial diffusion coefficients to be consistent with other harmonic approximations used in this work.

The defect formation enthalpy is calculated in pure Ni by comparing the energy of a cell containing the defect to that of an undefected cell (scaled to conserve the appropriate number of atoms). The *ab initio* vacancy and interstitial formation enthalpies are calculated using both the generalized gradient approximation (GGA) and the local density approximation (LDA). The *ab initio* results for the formation enthalpy of a ⟨1 0 0⟩ interstitial, H_{If}, in pure Ni are 4.07 eV for GGA and 4.60 eV for LDA. The authors are unaware of any existing experimental values reported for H_{If} in Ni. Other values in the literature for the formation enthalpy of a ⟨1 0 0⟩ interstitial in pure Ni range from 4.08 eV to 5.58 eV and were calculated using pair potentials and EAM potentials [29,67–70].

The enthalpy of vacancy formation, H_{vf}, in pure Ni has been measured experimentally. The experimental observations tend to fall into two groups, one around 1.5–1.6 eV and another around 1.7–1.8 eV (see Ref. [25] for a summary). Most measurements are performed using positron annihilation spectroscopy with various techniques of determining the vacancy formation enthalpy. Other values are reported from resistivity quenching measurements. Smedskjaer et al. [71] suggest that the discrepancy between the different experimental results could be due to uncontrolled metallurgical variables such as positron interactions with impurities or dislocations present in the sample. In light of the work by Smedskjaer et al., the commonly suggested experimental value is 1.79 ± 0.05 eV [25].

The *ab initio* results for vacancy formation enthalpies are 1.43 eV for GGA and 1.65 eV for LDA. The significant disparity between the GGA *ab initio* value and the experimental value for the vacancy formation energies is well known and likely due to surface effects, a problem that has been studied in detail by Mattsson et al. [72] and Carling et al. [73]. It is known that the LDA parameterization for the exchange–correlation energy minimizes these surface effects and better predicts vacancy formation energies. The LDA vacancy formation energy will therefore be used for a low temperature value to provide as accurate an *ab initio* value as possible. For the interstitial formation energy we will use the GGA value since interstitials do not create effective surfaces like vacancies and therefore should not have the same errors. All other *ab initio* parameters are calculated using GGA.

D.5. Migration barrier contributions

The migration barriers typically make the largest contribution to differences in diffusion coefficients due to the exponential dependence of diffusion on migration barriers. For this reason, the migration/rotation barriers are treated explicitly for all hops.

In the five-frequency model any associative or dissociative jump is assigned to the w_4 or w_3 rate, respectively. Since there are associative and dissociative jumps to and from the 2nd, 3rd and 4th nearest-neighbor positions, each with their own barrier, an effective rate is assigned to the associative and dissociative events. The effective rate is weighted by the number of pathways to each nearest-neighbor distance. Table D.2 contains the nearest-neighbor position, distance, multiplicity and different barriers for each distinct associative and dissociative pathway in the Ni–Cr and Ni–Fe system.

The separate w_3 and w_4 rates are each replaced with a single effective rate for application in the five-frequency model framework. An effective rate for the w_3 and w_4 events are calculated based on the discussion of KMC rate constants by Voter [74]. First consider dissociation (w_3). There are seven pathways for vacancy–solute dissociation, two to the 2nd nearest-neighbors, four to the 3rd nearest-neighbors and one to the 4th nearest-neighbors. The effective rate, w_{eff}^3, is determined by assigning the same rate to the seven dissociation pathways, which equals the sum of the rates for the three distinct dissociation pathways as shown in

$$7w_3^{eff} = 2w_3^{2nn} + 4w_3^{3nn} + w_3^{4nn} \tag{D.2}$$

This effective rate still maintains the total escape rate of the vacancy, w_{tot}, but by combining the dissociation events into a single rate allows for use in the five-frequency model. The total rate of escape is given by the following equation

$$\begin{aligned} w_{tot} &= 4w_1 + w_2 + 2w_3^{2nn} + 4w_3^{3nn} + w_3^{4nn} \\ &= 4w_1 + w_2 + 7w_3^{eff} \end{aligned} \tag{D.3}$$

The same approach can be used to determine an effective rate of association as well.

$$7w_4^{eff} = 2w_4^{2nn} + 4w_4^{3nn} + w_4^{4nn} \tag{D.4}$$

Table D.3 presents the migration barriers associated with the various frequencies for the vacancy tracer diffusion model. Note that we no longer explicitly write w^{eff} for effective rates but it is assumed that for any case with multiple hops a single effective rate is used. Table D.3 shows that the effective migration barrier for the

Table D.2
Migration barrier of associative and dissociative jumps.

Jump type	Nearest-neighbor position	Distance from solute (nm)	Multiplicity	Ni–Cr migration barrier (eV)	Ni–Fe migration barrier (eV)
w^3_{2nn}	2	0.351	2	1.02	1.07
w^3_{3nn}	3	0.430	4	1.04	1.08
w^3_{4nn}	4	0.496	1	1.04	1.05
w^4_{2nn}	2	0.351	2	1.05	1.07
w^4_{3nn}	3	0.430	4	1.06	1.07
w^4_{4nn}	4	0.496	1	1.14	1.11

Table D.3
Five-frequency model for vacancy diffusion in Ni–Cr and Ni–Fe.

Jump type	Ni–Cr migration barrier (eV)	Ni–Fe migration barrier (eV)
w_0	1.09	1.09
w_1	0.98	1.13
w_2	0.83	0.97
w_3	1.04[a]	1.07[a]
w_4	1.06[a]	1.07[a]

[a] Denotes an effective barrier.

Table D.4
Barriers for ⟨1 0 0⟩ interstitial model for tracer diffusion in Ni–Cr and Ni–Fe.

Jump type	Ni–Cr migration/rotation barrier (eV)	Ni–Fe migration/rotation barrier (eV)
w_0	0.14	0.14
w_{R0}	0.92	0.92
w_I	0.08	0.11
w_R	0.75	0.87
w_1	∞	0.16
w'_1	0.16	0.15
w_2	0.31	0.15
w'_2	0.00	0.20
w_3	0.26	0.14
w_4	0.15	0.20
w'_3	0.21	0.17
w'_4	0.10	0.15

w_3 and w_4 jumps would have been well approximated by the barriers of the most frequent pathway, the 3rd nearest-neighbor w^3_{3nn} and w^4_{3nn}, presented in Table D.2.

Table D.4 presents the migration/rotation barriers associated with the various rates needed to obtain the phenomenological coefficient of the interstitial model. Only a subset is needed to calculate tracer diffusion coefficients but all are given here for completeness. Note that the w'_2 barrier for Ni–Cr (hop from *a*-type first nearest-neighbor Cr to a Ni–Cr mixed dumbbell) is given as zero. There is essentially no barrier for this event, meaning that, any Ni–Ni dumbbell that becomes an *a*-type neighbor to a Cr atom would immediately collapse into a mixed dumbbell. The w_1 hop, which migrates from one *a*-type configuration to another, is therefore unstable in the Ni–Cr alloy and collapses into a mixed Ni–Cr dumbbell before it reaches the neighboring *a*-type site. Therefore, since the w_1 hop is not a viable pathway in the Ni–Cr alloy, it is assigned a barrier of ∞, corresponding to a rate of 0.

The diffusion models by Barbu [59] and Allnatt et al. [58] assume the associative and dissociative jumps, w_4 and w_3, respectively, to be between a first nearest-neighbor and a third nearest-neighbor (see Fig. B.2). The third nearest-neighbor has the highest multiplicity for interstitial association and dissociation. In the vacancy case the jump type with the highest multiplicity served as a good approximation for the effective rate. Therefore, for the interstitial case, the associative and dissociative jump barriers are approximated with the barriers between first and third nearest-neighbors and are given in Table D.4.

D.6. Binding enthalpy

The solute–defect binding enthalpies are calculated using what is sometimes called the indirect method. The indirect method calculates the binding energy with four different *ab initio* calculations where the energy of the defect and solute atom are subtracted separately from the energy of the system where they interact as first nearest-neighbors, and the method is described in detail in Refs. [75,76]. In this definition of binding enthalpy, a negative value denotes binding.

The vacancy–solute binding enthalpy is shown in Fig. D.1 for both Cr and Fe as a function of nearest-neighbor distance. Note that most solute–vacancy interactions are repulsive but in general all interactions are relatively weak and comparable to thermal energies even at room temperature. The first nearest-neighbor solute–vacancy binding enthalpies are about 0.5 eV for Cr and 0.2 eV for Fe (see Table 1). From Fig. D.1, it can be seen that the binding energy becomes quite small for the 5th and 6th nearest-neighbor but the 2nd, 3rd and 4th nearest-neighbors, which contribute to the effective rate of association and dissociation, still have some interaction energy with the solute.

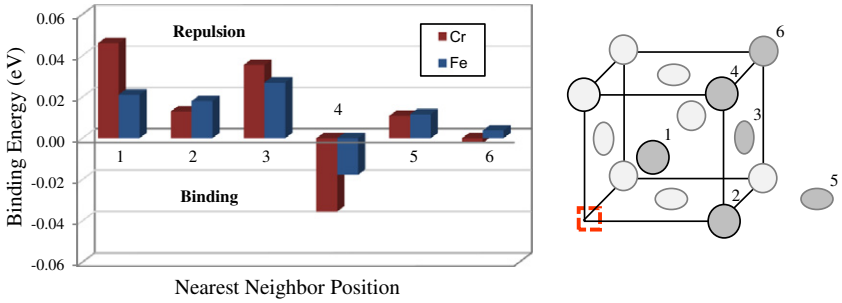

Fig. D.1. Solute–vacancy binding enthalpy vs. nearest-neighbor position.

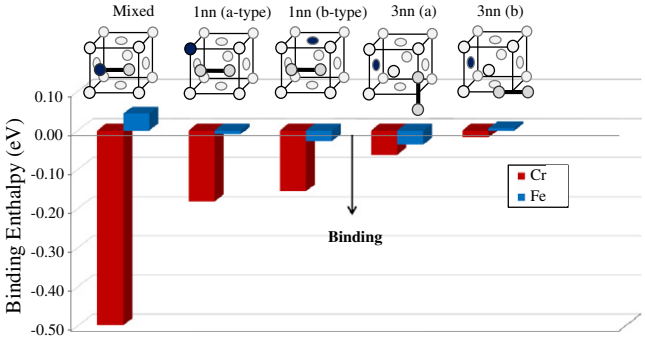

Fig. D.2. Solute–interstitial binding energy vs. nearest-neighbor position.

The binding enthalpies of solutes and interstitial dumbbells are also calculated using the indirect method. Fig. D.2 shows that there is significant binding between Cr and the interstitial in the mixed and first nearest-neighbor configurations. The *a*-type first nearest-neighbor binding enthalpies are used in calculating the diffusion coefficients. The binding between Cr and the interstitial is strong with a value of −0.18 eV and Fe–interstitial binding is weak with a value of −0.01 eV for Fe (see Table 4).

References

[1] E. Wimmer, W. Wolf, J. Sticht, P. Saxe, C.B. Geller, R. Najafabadi, G.A. Young, Phys. Rev. B (Condens. Matter Mater. Phys.) 77 (2008) 134305-1.
[2] A. Van der Ven, J.C. Thomas, Q.C. Xu, B. Swoboda, D. Morgan, Phys. Rev. B 78 (2008).
[3] G.S. Was, Fundamentals of Radiation Materials Science, Springer-Verlag, Berlin, Heidelberg, 2007.
[4] D.R. Olander, Fundamental Aspects of Nuclear Reactor Fuel Elements, Technical Information Center Energy Research and Development Administration, 1976.
[5] L.K. Mansur, Nucl. Technol. 40 (1978) 5–34.
[6] T.R. Allen, J.T. Busby, G.S. Was, E.A. Kenik, J. Nucl. Mater. 255 (1998) 44–58.
[7] C. Domain, J. Nucl. Mater. 351 (2006) 1–19.
[8] P. Olsson, J. Nucl. Mater. 386–388 (2009) 86–89.
[9] A.B. Lidiard, Philos. Mag. 46 (1955) 1218–1237.
[10] A.D. LeClaire, A.B. Lidiard, Philos. Mag. 1 (1956) 518–527.
[11] H. Eyring, M. Polanyi, Z. Phys. Chem. 12 (1931) 279–311.
[12] H. Eyring, J. Chem. Phys. 3 (1935) 107–115.
[13] A. Janotti, M. Krcmar, C.L. Fu, R.C. Reed, Phys. Rev. Lett. 92 (2004) 85901-1.
[14] M. Krcmar, C.L. Fu, A. Janotti, R.C. Reed, Acta Mater. 53 (2005) 2369–2376.
[15] G. Kresse, J. Furthmuller, Phys. Rev. B (Condens. Matter) 54 (1996) 11169–11186.
[16] G. Kresse, J. Hafner, Phys. Rev. B (Condens. Matter) 47 (1993) 558–561.
[17] J.P. Perdew, K. Burke, M. Ernzerhof, Phys. Rev. Lett. 77 (1996) 3865–3868.
[18] P.E. Blochl, Phys. Rev. B (Condens. Matter) 50 (1994) 17953–17979.
[19] G. Kresse, D. Joubert, Phys. Rev. B (Condens. Matter) 59 (1999) 1758–1775.
[20] J.D. Tucker, Ab Initio-Based Modeling of Radiation Effects in the Ni–Fe–Cr System, University of Wisconsin, Madison, 2008.
[21] G. Mills, H. Jonsson, G.K. Schenter, Surf. Sci. 324 (1995) 305–337.
[22] J. Askill, Tracer Diffusion Data for Metals, Alloys, and Simple Oxides, IRI/Plenum Data Corporation, New York, NY, 1970.
[23] C.J. Smithells, Smithells Metals Reference Book, eighth ed., Elsevier Inc., 2004.
[24] B. Million, J. Ruzickova, J. Velisek, J. Vrestal, Mater. Sci. Eng. 50 (1981) 43–52.
[25] P. Ehrhart, Atomic Defects in Metals, vol. 25, Springer-Verlag, Berlin, New York, 1991. pp. 88.
[26] M. De Koning, S. Ramos de Debiaggi, A.M. Monti, Diffus. Defect Data A Defect Diffus. Forum 224–225 (2004) 59–74.
[27] J. Ruzickova, B. Million, Mater. Sci. Eng. 50 (1981) 59–64.
[28] S.J. Rothman, L.J. Nowicki, G.E. Murch, J. Phys. F (Metal Phys.) 10 (1980) 383–398.
[29] S.R. de Debiaggi, M. de Koning, A.M. Monti, Phys. Rev. B 73 (2006) 104103-1.
[30] K.L. Wong, H.J. Lee, J.H. Shim, B. Sadigh, B.D. Wirth, J. Nucl. Mater. 386 (2009) 227–230.
[31] J.M. Perks, A.D. Marwick, C.A. English, Computer Code to Calculate Radiation-induced Segregation in Concentrated Ternary Alloys, AERE-R-12121, UKAEA Harwell, UK, 1986. pp. 48.
[32] J.M. Perks, S.M. Murphy, Modelling the Major Element Radiation-induced Segregation in Concentrated Fe–Cr–Ni Alloys, vol. 1, BNES, London, 1987. pp. 165.
[33] S. Watanabe, H. Kinoshita, N. Sakaguchi, H. Takahashi, J. Nucl. Mater. 226 (1995) 330–331.
[34] E.P. Simonen, M. Bruemmer, Radiation-induced Grain Boundary Segregation in Austenitic Stainless Steels, 1999, pp. 755.
[35] T.R. Allen, G.S. Was, Acta Mater. 46 (1998) 3679–3691.
[36] N.Q. Lam, A. Kumar, H. Wiedersich, in: H.R. Brager, J.S. Perrin (Eds.), Effects of Radiation on Materials: Eleventh Conference, Scottsdale, Arizona, American Society for Testing and Materials, Berlin, 1982, p. 985.
[37] N.Q. Lam, J. Nucl. Mater. 117 (1983) 106–112.
[38] S. Watanabe, N. Sakaguchi, K. Kurome, M. Nakamura, H. Takahashi, J. Nucl. Mater. 240 (1997) 251–253.
[39] M. Nastar, P. Bellon, G. Martin, J. Ruste, in: Proceedings of the 1997 MRS Fall Symposium, December 1–5, MRS, Warrendale, PA, USA, 1997, pp. 383 (Boston, MA, USA, 1998).
[40] R.G. Faulkner, International Workshop on Defect Production, Accumulation and Materials Performance in an Irradiation Environment, vol. 11, Elsevier, Davos, Switzerland, 1997. pp. 269.
[41] R.G. Faulkner, S. Song, D. Meade, C.C. Goodwin, Radiation-induced Grain Boundary Segregation, 1999, pp. 67.
[42] R.G. Faulkner, J. Mater. Sci. 16 (1981) 373–383.
[43] A.J. Ardell, Radiation-induced Solute Segregation in Alloys, Springer, Netherlands, 2008. pp. 285.
[44] J.D. Tucker, R. Najafabadi, T.R. Allen, D. Morgan, in: International Conference on Mathematics, Computational Methods and Reactor Physics (M&C 2009), Saratoga Springs, New York, May 3–7, 2009 (American Nuclear Society, LaGrange Park, IL, 2009).
[45] R.E. Stoller, J. Nucl. Mater. 276 (2000) 22–32.
[46] Jae-Hyeok Shim, Hyon-Jee Lee, B.D. Wirth, J. Nucl. Mater. 351 (2006) 56–64.
[47] G.R. Odette, M.J. Alinger, B.D. Wirth, Annu. Rev. Mater. Res. 38 (2008) 471–503.
[48] W.G. Wolfer, L.K. Mansur, J. Nucl. Mater. 91 (1980) 265–276.
[49] G. Ceder, Comput. Mater. Sci. 1 (1993) 144–150.
[50] N.W. Ashcroft, N.D. Mermin, Solid State Physics, first ed., Brooks Cole, 1976.
[51] C. Wolverton, A. Zunger, Phys. Rev. B (Condens. Matter) 52 (1995) 8813–8828.
[52] J. Callaway, Quantum Theory of the Solid State, Student ed., Academic Press, 1974.
[53] A.D. Le Claire, in: The International Conference on the Properties of Atomic Defects in Metals, 18–22 October, 1976, Argonne, IL, USA, 1978, pp. 70.
[54] A.R. Allnatt, J. Phys. C (Solid State Phys.) 14 (1981) 5467–5477.
[55] A.R. Allnatt, A.B. Lidiard, Atomic Transport in Solids, Cambridge University Press, 1993.
[56] J.L. Bocquet, G. Brebec, Y. Limoge, Diffusion in Metals and Alloys, Elsevier Science BV, Amsterdam, The Netherlands, 1996. pp. 535.
[57] M. Koiwa, S. Ishioka, Philos. Mag. A: Phys. Condens. Matter, Defects Mech. Prop. 47 (1983) 927–938.
[58] A.R. Allnatt, A. Barbu, A.D. Franklin, A.B. Lidiard, Acta Metall. 31 (1983) 1307–1313.
[59] A. Barbu, Acta Metall. 28 (1980) 499–506.
[60] J.R. Manning, Diffusion Kinetics for Atoms in Crystals, Van Nostrand, 1968.
[61] J. Bandyopadhyay, K.P. Gupta, Cryogenics 17 (1977) 345–347.
[62] S.M.1. Foiles, Phys. Rev. B (Condens. Matter) 49 (1994) 14930–14938.
[63] D.E. Jiang, E.A. Carter, Phys. Rev. B (Condens. Matter Mater. Phys.) 67 (2003) 214103-1.
[64] D.E. Jiang, E.A. Carter, Phys. Rev. B (Condens. Matter Mater. Phys.) 70 (2004) 64102-1.
[65] D.E. Jiang, E.A. Carter, Phys. Rev. B (Condens. Matter Mater. Phys.) 71 (2005) 45402-1.
[66] W. Schilling, J. Nucl. Mater. 69 (1978) 465–489.
[67] F. Gao, D.J. Bacon, G.J. Ackland, Philos. Mag. A (Phys. Condens. Matter, Defects Mech. Prop.) 67 (1993) 275–288.
[68] H. Sharma, S. Prakash, J. Phys. 60 (2003) 159–166.
[69] R.A. Johnson, Phys. Rev. 145 (1966) 423–433.
[70] S.M. Foiles, M.I. Baskes, M.S. Daw, Phys. Rev. B (Condens. Matter) 33 (1986) 7983–7991.
[71] L.C. Smedskjaer, M.J. Fluss, D.G. Legnini, M.K. Chason, R.W. Siegel, J. Phys. F (Metal Phys.) 11 (1981) 2221–2230.
[72] T.R. Mattsson, A.E. Mattsson, Phys. Rev. B (Condens. Matter Mater. Phys.) 66 (2002) 214110-1.
[73] K. Carling, G. Wahnstrom, T.R. Mattsson, A.E. Mattsson, N. Sandberg, G. Grimvall, Phys. Rev. Lett. 85 (2000) 3862–3865.
[74] A.F. Voter, Introduction to the Kinetic Monte Carlo Method, Springer, Dordrecht, The Netherlands, 2005.
[75] C. Domain, C.S. Becquart, Phys. Rev. B 65 (2002) 024103-1.
[76] J.D. Tucker, T.R. Allen, D. Morgan, in: Proceedings of the 13th International Symposium on Environmental Degradation of Materials in Nuclear Power Systems, August 19–23, 2007.